NASA TECHNICAL
MEMORANDUM

EFFECTS OF CAVITIES, PROTUBERANCES, AND REACTION-CONTROL JETS ON HEAT TRANSFER TO THE APOLLO COMMAND MODULE

by Robert A. Jones and James L. Hunt

Langley Research Center

Langley Station, Hampton, Va.
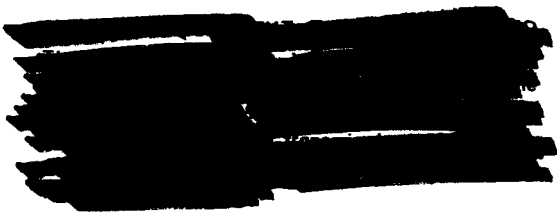
NASA TM X-1063

EFFECTS OF CAVITIES, PROTUBERANCES, AND

REACTION-CONTROL JETS ON HEAT TRANSFER TO THE

APOLLO COMMAND MODULE

By Robert A. Jones and James L. Hunt

Langley Research Center
Langley Station, Hampton, Va.

NATIONAL AERONAUTICS AND SPACE ADMINISTRATION

EFFECTS OF CAVITIES, PROTUBERANCES, AND

REACTION-CONTROL JETS ON HEAT TRANSFER TO THE

APOLLO COMMAND MODULE*

By Robert A. Jones and James L. Hunt
Langley Research Center

SUMMARY

An investigation was made in a conventional Mach number 8 facility to determine the effects of cavities, protuberances, and reaction-control jets on the heat transfer to the Apollo command module. A relatively new technique for obtaining quantitative aerodynamic heat-transfer coefficients was employed. In this technique the heat-transfer coefficients were determined by measuring the time required for the surface of the model to reach a known temperature as indicated by a visible phase change of a very thin surface coating.

Comparisons made herein of data obtained by this new method with data obtained with the conventional thermocouple-calorimeter technique show relatively good agreement. The detail obtained in interference regions indicate that this new method will be very useful for obtaining heat-transfer data on complex configurations. The data indicate considerable increases in heating due to interference in various regions; the presence of shear pads caused increases by factors of about 2, a small region immediately ahead of the umbilical fairing experienced a heating rate that may have been 8 to 10 times that of a smooth body, the antenna on the windward afterbody caused increases as high as 6, and the reaction-control jets caused increases as high as 11 in one instance. There were no large effects of afterbody cavities on the heat-transfer rate in the separated portion. It is believed that the sting-interference effects in this region may have been larger than any effects of cavities or protuberances.

INTRODUCTION

In cooperation with the NASA Manned Spacecraft Center, an investigation has been made in the Langley Mach 8 variable-density tunnel to determine the interference heating rates in the vicinity of cavities, protuberances, and reaction-control jets on the Apollo command module. A relatively new phase-change coating technique which has been developed at Langley for determining aerodynamic heat-transfer data on complex configurations was used. The various phases

---

*Title, Unclassified.

of this investigation were conducted between November 1963 and March 1964. Data were obtained at free-stream Reynolds numbers based on model diameter ranging from 0.13×10^6 to 1.5×10^6. The purpose of this paper is to make available the results of this investigation.

SYMBOLS

A	phase-change temperature
$\hat{A}$	temperature factor, $\dfrac{A - T_i}{T_{aw} - T_i}$
c_p	specific heat at constant pressure
D	diameter of face of model
h	heat-transfer coefficient, $Btu/ft^2 sec\,^oR$
h_c	heat-transfer coefficient as determined by a constant thermal property solution (eq. (5))
h_o	stagnation-point heat-transfer coefficient at angle of attack (taken as measured value of ref. 5)
h_v	heat-transfer coefficient as determined by variable thermal property solution (ref. 4)
$\bar{h}$	maximum ratio of heat-transfer coefficient with interference to heat-transfer coefficient without interference
k	thermal conductivity
l	depth of heat penetration
M_∞	free-stream Mach number
p	parameter, $\dfrac{h}{k}\sqrt{\alpha t}$
p_j	stagnation pressure of reaction-control nozzle
p_t	stagnation pressure
$p_{t,2}$	stagnation pressure behind normal shock
r_a	radius of afterbody
r_c	radius of corner

2

r_n radius of curvature of face

r_s radius of sting

$R_{\infty,D}$ Reynolds number based on free-stream conditions and model diameter

s surface distance measured from center of face

T temperature

T_1 initial temperature

T_{aw} adiabatic wall temperature

t time

t_d thermal diffusion time

u_∞ free-stream velocity

x distance normal to surface

α thermal diffusivity, $\dfrac{k}{\rho c_p}$

ρ density

FACILITY

All the data presented herein were obtained in the Langley Mach 8 variable density tunnel. This facility has a contoured axisymmetric nozzle with an 18-inch-diameter test section. It is especially adapted for transient testing by means of a model injection mechanism located directly beneath the test section. Windows are located on both sides and the top of the test section for lighting and photographing the model. The Mach number calibration of the test section for the range of Reynolds numbers of this investigation is shown in the following table:

$R_{\infty,D}$	M_∞
0.2×10^6	7.70 ± 0.05
0.5	7.86 ± 0.02
1.5	7.95 ± 0.03

A total of four different models were used in this investigation. For all the models the areas where heat-transfer data were to be obtained were made from a high-temperature fiber-glass-reinforced plastic material. The thermophysical properties (specific heat, thermal conductivity, and density) were measured on samples of this material by a private corporation under contract with Langley. The quoted accuracy of these data was: specific heat, ±2 percent; thermal conductivity, ±3 percent; and density, ±1 percent. The values of these properties for various temperatures are shown in the following table:

T, $^{\circ}$F	ρ, lb/cu ft	c_p, Btu/lb-$^{\circ}$F	k, Btu/ft-sec-$^{\circ}$F	α, ft^2/sec
75	119.1	0.1987	0.77×10^{-4}	3.25×10^{-6}
100	118.7	.2163	.79	3.07
125	118.3	.2288	.78	2.89
150	117.8	.2369	.80	2.87
175	117.4	.2545	.80	2.68
200	116.9	.2994	.83	2.37
225	116.5	.2699	.83	2.64
250	116.1	.3055	.84	2.37

The effect of the variation of these properties on the data will be discussed later.

A sketch of model 1 is shown in figure 1. This model had a steel afterbody and two interchangeable faces made of the plastic material. One face was smooth and the other had three shear pads as shown in the sketch. The minimum thickness of plastic on the face was 1/4 inch. Model 1 was used only for data on the face at an angle of attack of 35°.

Model 2 was a smooth model constructed entirely of plastic. (See fig. 2.) The sting shown in figure 2 was also used with models 3 and 4.

Model 3 was made entirely of plastic and made to scale of the Apollo command module. Photographs of several different views of this model are presented in figure 3. The shear pads on the face of this model were located as shown in figure 1; however, all three pads had the same height, 0.016 inch. The tension ties, located adjacent to the shear pads, are shown in these photographs as longer than they were when the model was tested. These tension ties were filed down to a length of 0.040 inch after these photographs were made. The cavities and protuberances on the afterbody are the antennas, cabin vent, umbilical fairing, crew hatch, rendezvous and docking windows, and escape tower wells.

Model 4 was used to study the effect of the reaction controls. A sketch of this model is shown in figure 4. The model was made with a steel core and a 1/16-inch layer of plastic on the conical portion of the afterbody. Two

different reaction-control nozzles were used with this model; one had a throat diameter of 0.080 inch and the other had a throat diameter of 0.020 inch. Each nozzle had a conical expansion section with a 5° half-angle. The locations of the threaded holes to receive the nozzles and the air ducts to the holes are shown in figure 4(a). The nozzles could be screwed in place in either location or they could be removed and the hole plugged. By varying the roll angle of the model, the roll nozzle (hole 1) could be placed so that it exhausted either forward (into the wind) or aft with an angular location in both cases of 133° from the windward afterbody ray. The other hole (hole 2) location could be used as a yaw nozzle located 92° from the windward ray or as a pitch nozzle located 182° from the windward ray. For clarity, sketches showing the relative orientation of the nozzle thrust vector with the free stream are presented in figure 4(b) for each configuration tested.

Dry room-temperature air was introduced through a hole in the sting to the plenum chamber inside the model. The pressure in the plenum chamber was measured and the mass flow of air through the nozzle was also measured to make certain that sonic flow existed at the throat of the nozzle. The face of this model was covered with sandpaper-type three-dimensional roughness of about 0.015-inch maximum height. There were no cavities or protuberances on this model other than the nozzles and roughness.

METHOD OF OBTAINING HEAT-TRANSFER COEFFICIENTS

Heat-transfer coefficients were obtained by using a phase-change coating technique which has been developed at the Langley Research Center to obtain quantitative data on complex shapes. This technique employs a coating of material which undergoes a visible phase change from an opaque solid to a clear liquid at a known temperature. The times for which the change occurs for various locations on the model are determined by motion-picture photography. The patterns so obtained represent lines of constant surface temperature. If the depth of heat penetration is small compared with model dimensions, then these patterns also represent lines of constant heat-transfer coefficient. The value of the heat-transfer coefficient is obtained from solutions of the transient, one-dimensional heat-conduction equation. A brief description of this method was given in reference 1.

Phase-Change Coating

The coating materials that were used (see refs. 1 and 2) undergo a phase change from a solid to a liquid at known temperatures. The materials available have phase-change temperatures that differ as little as 3° F and cover a range from 100° F to 2500° F, each indicating a specific temperature with a tolerance of ±1 percent. The materials used in this investigation had phase-change temperatures of 113°, 125°, 150°, 175°, 200°, 225°, and 250° F.

The materials as supplied by the manufacturer were suspended in an inert, volatile, nonflammable vehicle which can be mixed with a special thinner and

sprayed on the model. When the model is sprayed with a very thin (less than 0.001 inch) coat of this material, it appears to be covered with small opaque white crystals. When the coating melts, it becomes transparent and good contrast between the melted and unmelted region can be obtained if the surface of the model is dark colored. With care, the coating can be made sufficiently thin so that the running of the melted material and the errors due to the latent heat of melting are negligible and yet the contrast is adequate for black and white photography. A comparison of data obtained with this phase-change coating method with data obtained with the conventional thermocouple-calorimeter method is given subsequently.

In order to ascertain the effects of heating rate and pressure on the temperature required for a phase change, a calibration apparatus was built; this apparatus allowed the accurate measurement of phase-change temperature for a wide range of heating rates and ambient pressures. The apparatus consisted of a thin stainless-steel plate instrumented with thermocouples on the top surface and heated from below by a radiant heat source. The temperatures were recorded on magnetic tape by a high-speed analog to digital converter. The progressions of the isotherms over the plate were photographed with a 35-millimeter time-study motion-picture camera. Electrical circuits for the recorder and camera were synchronized for a simultaneous start and thus provided a reference time for the two sets of data. The time, surface temperature, and rate of change of surface temperature with time for which the phase change occurred at each thermocouple were obtained from the data. Sample photographs of the phase-change patterns on the calibration plate are shown in figure 5. The phase change is taking place at the line separating the light and dark areas. The melted portion or dark area was subjected to the higher heating rates.

Calibration tests were made for various heating rates in which the rate of change of surface temperature ranged from approximately 1° F per second to 75° F per second at atmospheric pressure. Pressure effects were determined by placing the calibration apparatus in a bell jar and repeating the procedure for pressures as low as 1 millimeter of mercury absolute. The effect of pressure and heating rate on the phase-change temperature was found to be negligible for the materials used in these tests.

Test Technique

The first step in the test procedure was to photograph a model on which a grid had been painted. This model was placed in the exact position where the test model was to be placed. Then the test model was sprayed with the coating material and mounted on the model injection mechanism which was in the retracted position so that during the tunnel starting period, the model was not exposed to the air stream and thus remained isothermal. The tunnel was started and brought to the desired operating conditions. The camera and lights were then started and the model was rapidly injected into the steady air stream. The injection time, that time from which the model first encounters the tunnel boundary layer until it is positioned in the uniform flow, was about 0.05 second. Between runs the model was taken out of the tunnel, the phase-change material was washed off with thinner, the model was cooled by ice water, the

temperature was monitored, sufficient time was allowed to let the model reach an isothermal room-temperature condition, and then the model was sprayed with a new coat of phase-change material. Lines of constant heat-transfer coefficient were located by superimposing the phase-change patterns on the grid photographs.

All data were recorded on high-speed 35-millimeter black and white film using a special data camera and stroboscopic flash lamps. This camera is driven by a synchronous motor through interchangeable gears which allow exact framing rates of either 10, 20, or 30 frames per second. It is also equipped with two timing lights which can be used to put marks on the film margin for time correlation. The negatives are exposed in a double-frame format about 24 millimeters by 36 millimeters in size. The model was lighted and photographed through windows in the test section. A photograph of a typical test setup is presented in figure 6.

Since the model must be made from a good insulating material (more will be said about this later), care had to be taken to avoid errors due to radiation. The walls of the tunnel test section remain at nearly room temperature during the test and the temperature at which the phase change occurs is low so that radiation from these sources was negligible. However, it was found that radiation from photoflood lights could introduce a considerable error. Photoflood lights set at an intensity suitable for photography were found to melt the lower temperature phase-change coatings in approximately 10 seconds which was of the same order of time as that for some of the lower aerodynamic heat-transfer rates. This problem was eliminated by the use of high-intensity electronic strobe lights which were synchronized with the camera shutter. Although these lights had a high intensity, the duration of a single flash was only 25 microseconds so that the total "on-time" of the lights at the highest framing rate was only 0.75×10^{-3} seconds per second of test time or less than 0.1 percent.

Theory for Heat-Transfer Coefficients

In the method described here, the heat-transfer coefficients depend on the time required for the phase change to occur and the thermal properties of the model material. The equation describing the transient one-dimensional flow of heat is:

$$\frac{\partial T}{\partial t} = \alpha \frac{\partial^2 T}{\partial x^2} \tag{1}$$

with the initial and boundary conditions which most nearly describe the actual tunnel transient test:

$$T(x, 0) = T_i \tag{2}$$

$$T(\infty, t) = T_i \tag{3}$$

7

$$\frac{\partial T(0,t)}{\partial x} = \frac{h}{k}\left[T_{aw} - T(0,t)\right] \tag{4}$$

Now it is assumed that the phase-change coating is at the surface temperature $T(0,t)$ and the value of time t is required when $T(0,t) = A$ (A is the temperature at which the phase change occurs). Other assumptions are: (1) that the depth of heat penetration into the wall is small compared with the wall thickness so that the wall acts like a semi-infinite slab (eqs. (1) and (3)); (2) that the model is isothermal before injection into the air stream (eq. (2)); (3) that the aerodynamic heat-transfer coefficient h is invariant with time (eq. (4)) which is a condition normally encountered in the wind tunnel with constant stagnation conditions and a laminar boundary layer.

The solution of equation (1) is given in reference 3 (p. 72) and with the stated boundary conditions can be written in terms of parameters of interest here as:

$$\hat{A} = 1 - e^{p^2} \operatorname{erfc} p \tag{5}$$

where

$$\hat{A} = \frac{A - T_1}{T_{aw} - T_1} \tag{6}$$

$$p = \frac{h}{k}\sqrt{\alpha t} \tag{7}$$

The solution of equation (5) is plotted in figure 7 in terms of the parameter p as a function of $\hat{A}$. The parameter p is a function of the properties of the wall material, the aerodynamic heat-transfer coefficient, and the time required for the phase change to occur. For a given set of conditions and a known time for the phase change, the value of the heat-transfer coefficient can be computed from equation (7). An alternate way of plotting the solution of equation (5) is presented in figure 8. In this figure the parameter h/k is plotted as a function of time for various values of $\hat{A}$. If the model properties are known, the value of the heat-transfer coefficient can be read directly from figure 8; however, this procedure requires interpolation between the different values of $\hat{A}$.

The time required for the phase change to occur should be large compared with the time required for the model to reach the proper location in the tunnel in order to minimize errors due to the erroneous heat-transfer rates encountered while the model is passing through the tunnel boundary layer and errors due to the accuracy of determining the initial time. However, the time required for the phase change to occur should be short compared with the thermal diffusion time of the model. This thermal diffusion time t_d is approximately independent of the aerodynamic heat-transfer coefficient and depends only on the thermal diffusivity of the model material and the allowable depth l of

heat penetration. The thermal diffusion time is given approximately by the equation:

$$\frac{\alpha t_d}{l^2} \approx 0.2 \tag{8}$$

This equation was obtained by assuming a cubic distribution of temperature with depth in a slab subjected to an instantaneously applied constant heat-transfer rate at one surface and solving for the value of the parameter $\alpha t_d / l^2$ for which the back surface first experienced a noticeable change in temperature. In practice, the time required for the phase change to occur can be controlled by selecting a coating with a suitable value of A. It may sometimes be desirable to coat different areas of a model with coatings having different values for A. The value of l should be small compared with a model dimension for which accurate data are required, for example, nose or corner radius. To insure reasonably small values for l, the model should be made from a material having a very low thermal conductivity. A very low thermal conductivity also minimizes the lateral conduction along the surface.

In order to check both the usefulness of the infinite slab solution (eq. (5)) and the method given previously for determining the depth of heat penetration (eq. (8)), a computation was made for the actual slab thickness and model material used in this investigation. This computation was made by the numerical analysis method of reference 3 for a slab thickness of 1/4 inch, an aerodynamic heat-transfer coefficient of 0.001, an initial temperature of 75° F, and an adiabatic wall temperature of 940° F. The thermophysical properties of the slab material were:

$$\rho = 117.6 \text{ lb/ft}^3$$

$$c_p = 0.2163 \text{ Btu/lb}^\circ\text{F}$$

$$k = 0.79 \times 10^{-4} \text{ Btu/ft sec}^\circ\text{F}$$

The resulting temperature-time variation of the front and back surface is shown in figure 9. Note that the front surface temperatures for the infinite slab and 1/4-inch-thick slab are nearly identical for times as long as 35 seconds. For the same material properties and slab thickness, equation (8) gives a thermal diffusion time of 29 seconds. Equation (8) is therefore a conservative value for thermal diffusion time or allowable depth of heat penetration. In other words for these test results, equation (5) should give accurate heat-transfer coefficients for times as long as 35 seconds in regions away from the corners or protuberances. The heat-transfer data in the vicinity of the shear pads, tension ties, and so forth were obtained at times much less than 35 seconds, more nearly 1 to 2 seconds, and the depth of heat penetration is very small; therefore, the data in the immediate vicinity of a protuberance (up to 0.03 inch) should be accurate.

The thermophysical properties of the model material given previously varied considerably with temperature. In the solution to the heat conduction equation,

the material properties appear as the parameter $\sqrt{\alpha}/k$. (See eq. 7.) For the data of this report the value of $\sqrt{\alpha}/k$ was always taken to be the average value for the temperature range from 75° F, approximate initial temperature, to the temperature of phase change A. These values were:

A$^\circ$ F	$\sqrt{\alpha}/k$, ft^2(sec)^2 $^\circ$F/Btu
113	22.8
125	22.6
150	22.4
200	21.0

In order to evaluate the errors which are due to the variation of material properties $\left(c_p \text{ and } k\right)$ with temperature, the numerical analysis method of reference 4 was used to obtain heat-transfer coefficients for the actual variable properties listed previously by interpolating linearly between the eight temperatures for which the properties were measured. The heat-transfer coefficients determined in this manner for temperature-dependent properties are compared with values from equation (5) in figure 10. The data are shown as the ratio of heat-transfer coefficients determined from the temperature-dependent properties finite-thickness solution h_v (ref. 4) to the heat-transfer coefficients determined from the constant-property finite-slab solution h_c (eq. (5)) as a function of time. The data are shown for several values of phase-change temperature and various heat-transfer coefficients ranging from 0.001 to 0.01. It is thought that the effects of the variation in thermophysical properties with temperature shown in figure 6 are small enough to be considered negligible.

RESULTS AND DISCUSSION

Face Data

The heat-transfer data of the smooth face model (model 1 at an angle of attack of 35°) are shown in figure 11 and compared with data obtained by the thin-skin thermocouple-calorimeter data of reference 5. The data of reference 5 were obtained in the same facility at the same test conditions. These two sets of data show relatively good agreement for the two different methods of obtaining heat-transfer coefficients.

An effect of the shear pads on the heat-transfer distribution on the face can be seen in figure 12. These photographs were taken during a test of model 1. The flow direction is from left to right so that the stagnation point is located at the left side of each photograph. The dark areas of the photograph are areas in which the phase change has occurred and consequently represent regions of higher heat-transfer rate than the light areas. The amount of detail as to the heat-transfer distribution in the interference region indicates that this method will be very useful for obtaining heat-transfer data on complex configurations. The actual coefficients which were determined from

patterns such as these are shown in figures 13, 14, and 15. The photographs of figure 12 and all other photographs shown herein are only samples and do not necessarily correspond to the same times as the patterns in the sketches. Also in all the sketches of heat-transfer patterns, the shaded portion represents the unmelted coating and therefore the area of lower heat-transfer rate. The values of heat-transfer coefficient are given for each sketch in units of $Btu/ft^2 sec °R$ and apply to the line separating the light and shaded areas. Also shown in these figures are the nondimensional heat-transfer ratios h/h_0 where h_0 is the angle-of-attack stagnation-point heat-transfer coefficient taken from reference 5. These patterns as well as all others presented in this report were traced directly from enlargements of the film and show a distorted view of the surface because of the angle between the camera and model. The horizontal line through the sketches represents the vertical line of symmetry of the face. The dimensionless coordinates s/r_n are shown in figure 13(i).

A comparison of the heat-transfer distribution along the vertical plane of symmetry from figure 13 with that for the smooth-face configuration shown in figure 11 indicates no effect of the shear pads on the heat-transfer rate along this line for values of s/r_n greater than zero. However, in the immediate vicinity of the windward shear pad, the data of figure 13(a) show heat-transfer coefficients about twice as high as those measured at the same location in reference 3. If an interference heating factor $\bar{h}$ is defined as the maximum ratio of heat-transfer coefficient with interference to the heat-transfer coefficient without interference, it would have a value of about 2 in this region. For the rearward shear pad (fig. 13(f)), $\bar{h}$ would be about 1.3. The effect of increasing Reynolds number on the heat-transfer rates in the vicinity of the shear pads can be seen by comparing figures 13, 14, and 15.

From the patterns shown in figures 13, 14, and 15, it appears that the relative nondimensional levels of heat transfer in the vicinity of the windward shear pads are not affected greatly by Reynolds number, but that larger areas are affected at the higher Reynolds numbers. In figures 13(a) and 14(a), for example, the levels h/h_0 are about the same but a considerably larger area downstream of the windward shear pads is affected at the higher Reynolds number of figure 14(a). This result may be misleading in that at the higher Reynolds numbers the phase change occurs more rapidly; therefore, the patterns at the earliest time for which data can be reduced have progressed farther. Therefore, in figure 14(a) a small region inside the phase-change area could have heating rates higher than those indicated. If it is assumed that the interference heat-transfer patterns at both Reynolds numbers were formed in a similar fashion, the distributions for the test in figure 14 at earlier times would appear as shown in sketch (a) for pad 1. The nondimensional levels h/h_0 of 1.7 and 1.2 correspond to interference heating factors $\bar{h}$ of 2.9 and 2, respectively. The conclusions that must be drawn from the data of figures 13, 14, and 15 as to the effects of Reynolds number on interference heating at the windward shear pads are therefore: (1) an increase in Reynolds number caused a larger area to be affected, and (2) the possibility exists that the maximum nondimensional value h/h_0 may have been higher for high Reynolds numbers. The effects of Reynolds number are probably associated with changes in flow patterns around the shear pads due to changes in boundary-layer thickness relative to the shear-pad height.

$$\frac{h}{h_0} = 1.2$$

$$\frac{h}{h_0} = 1.7$$
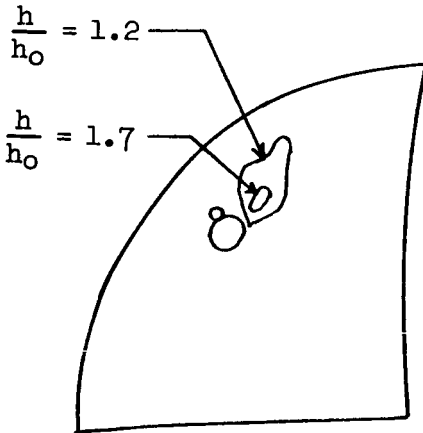
Sketch (a)

The Reynolds number effect on the interference heating patterns in the vicinity of the leeward shear pad indicate a much more drastic change in local flow pattern than for the windward shear pads. The low Reynolds number patterns (fig. 13) indicate that the interference effects are confined to a region immediately in front of and extending directly behind the pad. The highest Reynolds number pattern (fig. 15(b)) shows an increase in heat transfer which is confined to a narrow band well in front of and on either side of the shear pad.

The data obtained in the vicinity of the leeward shear pad of model 3 are interesting to compare with the results discussed previously in that the height of this pad was only 42 percent of that of the leeward pad on model 1. Enlargements of photographs taken during a test of model 3 are presented in figure 16. Only the leeward half of the face was coated for these tests; thus, no phase-change patterns appear on the windward half. The pattern for the earliest time of figure 16 is therefore only meaningful in the vicinity of the shear pad and umbilical fairing. The heat-transfer-coefficient distribution for this same Reynolds number is shown in figure 17 and the highest Reynolds number data are shown in figure 18. Model 3 was tested at an angle of attack of 33° as compared with an angle of attack of 35° for model 1; however, the effects of this difference are thought to be small compared with the effects of the large difference in shear pad height. The entire face except for the region near the shear pad is shown shaded in figures 17(a) and 18(a), since the windward half of the face was not coated. The bow-shock type of pattern of figure 15(b) is not present for the high Reynolds number patterns with the shorter shear pad. (See fig. 18.) The interference heating factor $\bar{h}$ in the vicinity of the leeward shear pad (figs. 17 and 18) is about 2 and is somewhat larger than that for model 1 even though the pad height was less than half that of model 1.

Figures 17 and 18 show a region of high heat transfer immediately ahead of the umbilical fairing. No heat-transfer data were obtained in this region for a smooth configuration either in this investigation or in reference 4. The smooth-body heat-transfer rates in this area should be decreasing very rapidly with distance away from the stagnation point so that the increase due to interference from the umbilical fairing may be very large. A comparison with some unpublished data obtained from John Bertin of the NASA Manned Spacecraft Center for a smooth body indicates the increase in heat transfer for the small region immediately ahead of the umbilical fairing may be as large as 8 to 10 times that of the smooth body.

The heat-transfer distribution along the windward ray of the smooth after-body, model 2, is shown in figure 19 and compared with the thermocouple-calorimeter data of reference 5. Although the test conditions for these two sets of data were approximately the same, there were slight differences in the geometry of the models. The model used for the phase-change data had an after-body angle of 33° whereas the model of reference 5 had a 35° afterbody angle. However, the angles of attack for the two sets of data were such that the wind-ward afterbody ray was alined parallel to the free-stream flow direction in both cases so that the effect of model differences should be small. Figure 19 shows the phase-change data to be as much as 30 percent higher than the thermo-couple data. Consideration of differences in the model geometry and possible errors in both methods indicates that this discrepancy is feasible.

Sketches of the smooth-body heat-transfer patterns from which the phase-change data of figure 19 were taken are shown in figure 20. The heat-transfer patterns for the model with antenna and tower wells, model 3, are shown in fig-ure 21. The heating rates in the vicinity of the antenna (fig. 21(b)) are approximately 6 times the values for the smooth configuration ($\bar{h} \approx 6$). The presence of the antenna caused increased heating rates over a large portion of the windward afterbody (figs. 21(e) and 21(f)).

The distribution of heat transfer along the vertical plane of symmetry as obtained from figure 21 for the windward corner, figure 19 for the windward afterbody, and figure 11 for the face is shown in figure 22. The thermocouple-calorimeter data of references 5 and 6 are also shown. All these data are nondimensionalized by the measured stagnation-point values of reference 5. The data for the corner and afterbody were taken at an angle of attack of 33° with an afterbody angle of 33°; however, the data for the face were taken at an angle of attack of 35°. No heat-transfer data were obtained in references 5 and 6 in the corner region as the lateral conduction was large and the corner radius was too small to instrument with thermocouples. In the phase-change data, however, lateral conduction is negligible because of the extremely low thermal conductivity of the plastic. Therefore, although the data of figure 22 are for two slightly different angles of attack, they are useful in that they show the distribution in the corner region. The peak measured heat-transfer rate at the corner was 1.55 times the stagnation-point value; however, it is possible that higher rates may exist in the region $0.41 < s/r_n < 0.43$ as no data were obtained there.

Leeward Afterbody Data

The heat-transfer distribution along the leeward afterbody ray of the smooth model is shown in figure 23 and compared with the data from reference 6. There is a considerable difference between these two distributions which is believed to be the result of the different model supports used in the two investigations. In addition to the difference in model supports, there was a 2° difference in the afterbody angle of the models. This small difference was thought to have negligible effects compared with the model support effect.

The model of reference 6 was supported by a strut attached to the windward ray of the afterbody near the forward corner while the model of this investigation was supported from the rear of the afterbody by a sting as shown in figure 8. In the investigation of reference 6, data were taken with several different struts for zero angle of attack and the strut interference was found to have considerable effect on the afterbody heat-transfer distribution. The data of reference 6 also show the different struts caused variations in peak afterbody heat-transfer rate by more than 50 percent. The strut variations of reference 6 are shown in sketch (b). None of the strut configurations of reference 6 are similar to the sting used in the present investigation.

Sketch (b)
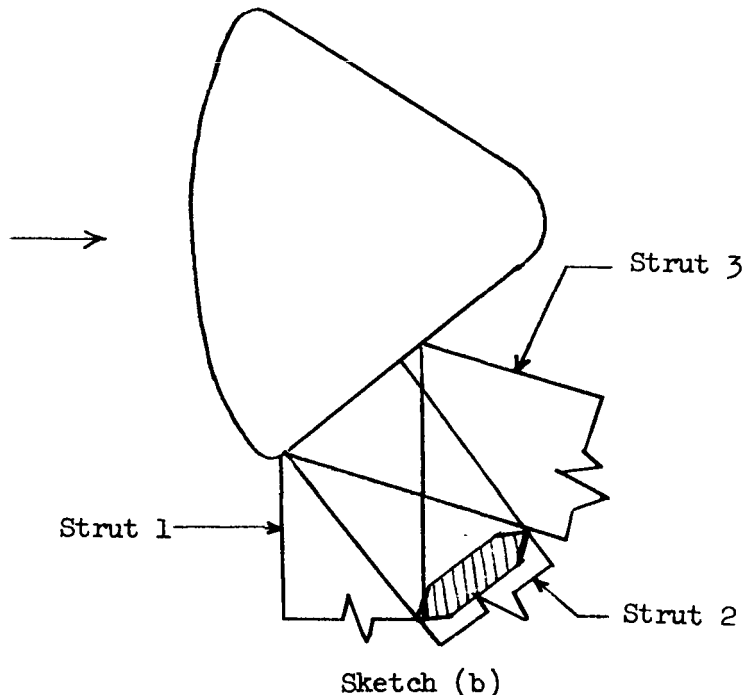
The heat-transfer patterns on the smooth leeward afterbody are presented in figures 24 and 25; the patterns for the leeward afterbody with cavities and protuberances are presented in figures 26 and 27. The photographs of figure 26 were made with a telephoto lens so that only a portion of the model filled the entire 35-millimeter frame. The different cavities and protuberances are labeled in the sketch of figure 26(c) and the nondimensional surface distance s/r_n along the most leeward ray is shown. A comparison of figures 25 and 27 indicates that the heat-transfer rates are not greatly affected by the presence of the cavities and protuberances except for two small areas. One of these areas is in the vicinity of the umbilical fairing; the other is directly ahead of the window located behind the vent. The heat transfer to these two areas may have been increased by 50 percent. However, the distribution and interference effects of a free-flight vehicle may be entirely different in this separated afterbody region.

Reaction-Control Data

The reaction-control effects on afterbody heat transfer were determined by using model 4 at an angle of attack of 35°. As described in the model section, the layer of plastic on the afterbody was necessarily rather thin (1/16 inch) in order to allow installation of the nozzles; therefore, the time for which the plastic layer acts as a semi-infinite slab is short, that is, the thermal diffusion time t_d is about 2 seconds. For times longer than about 2 seconds, the surface temperature of the plastic "feels" the steel core of the model and the theoretical solutions for the surface temperature of equation (5) are not valid. Even though the infinite-slab solutions are not valid for times longer than 2 seconds, the phase-change patterns do represent lines of constant heat-transfer coefficient. Therefore, for a given pattern, if the coefficient can be determined for a line not affected by the reaction controls, the coefficient is known for the entire pattern. These coefficients can be determined by comparison with thermocouple-calorimeter data at the same test conditions. Because of the low heating rates of these tests, some of the phase-change patterns were obtained at times longer than 2 seconds and the heat-transfer coefficients for these cases were obtained by comparison with the data of reference 6 where possible.

The remaining figures (figs. 28 to 39) present the heat-transfer patterns on the afterbody of model 4. For all the data with the reaction-control jets, the face of the model was covered with sandpaper type of roughness of 0.015-inch maximum height. A list of test conditions and maximum values of interference heating factor $\bar{h}$ for each figure is given in the following table:

Figure	$R_{\infty,D}$	Reaction-control jet	$p_j/p_{t,2}$	p_t, psia	p_j, psia	$\bar{h}$
28(a)	0.13×10^6	0.08 inch; yaw	259	95	215	
28(b)	1.5	0.02 inch; forward roll	58	1020	515	
28(c)	1.5	0.02 inch; aft roll	58	1015	515	
29(a)	.5	None		315		
29(b)	1.5	None		1020		
30	1.5	0.08 inch; yaw	25	1005	215	4
31	.13	0.08 inch; yaw	259	95	215	2.5
32	.13	0.02 inch; yaw	621	95	515	2
33	1.5	0.02 inch; yaw	59	1005	515	4
34	1.5	0.02 inch; pitch	58	1010	515	1
35	1.5	0.02 inch; yaw; forward roll	58	1015	515	4
36	1.5	0.02 inch; forward roll	59	1020	515	4
37	.13	0.02 inch; forward roll	606	97	515	11
38	.13	0.02 inch; aft roll	606	97	515	3
39	1.5	0.02 inch; aft roll	58	1015	515	3

In the column labeled reaction-control jet, the diameter of the throat of the nozzle is listed followed by the orientation of the jet, that is, yaw, forward firing roll, aft firing roll, or pitch. The jet pressure ratio $p_j/p_{t,2}$ is

the ratio of the stagnation pressure of the reaction-control nozzle to the pressure at the stagnation point of the model. The interference heating factor $\bar{h}$ is the ratio of maximum heat-transfer coefficient in the vicinity of a reaction-control jet to the heat-transfer coefficient for the no-interference condition at the same location. The no-interference data were obtained from reference 6. Since the exact locations are difficult to determine from the phase-change patterns and since the no-interference data were obtained by interpolating between thermocouple stations in reference 6, these interference heating factors are only approximate.

Photographs of the model in the test section are shown in figure 28 for each of three different reaction control jets. The heat-transfer patterns in these photographs indicate that the interference from the jets affected a rather large portion of the afterbody surface. In general, the reaction controls caused an increase in heat transfer for all conditions. The one exception was the pitch jet. (See fig. 34.) For this jet there were no noticeable interference effects. The data of figures 30 to 34 indicate peak interference heating factors of about 4 for the yaw jet. This interference heating factor for the yaw jet was always larger for the high Reynolds number low jet pressure ratio condition. The data for the forward firing roll jet (figs. 36 and 37) show just the opposite trend with a peak interference heating factor of 11 at the low Reynolds number high jet pressure ratio condition. The aft firing roll jet (figs. 38 and 39) caused increases in heat transfer by about 3 that were independent of Reynolds number and jet pressure ratio.

It seems probable to expect that the interference patterns on the afterbody caused by the reaction-control jets indicate regions of increased pressure as well as increased heat transfer. If this is actually the case, then for some of the patterns shown the moments caused by the jet thrust may be partially offset or augmented by moments caused by the mutual interference of the jet and local flow and cross-coupling of yaw, roll, and pitch moments would exist. There is no way of determining from these results what the pressure in the interference regions would be; however, the patterns show that a rather large area on the afterbody is affected and further investigation of this problem appears to be desirable.

SUMMARY OF RESULTS

An investigation was made in a conventional Mach number 8 facility to determine the effects of cavities, protuberances, and reaction-control jets on the heat transfer to the Apollo command module. A relatively new phase-change coating method was used for determining the aerodynamic heat-transfer coefficients. The results of this investigation may be summarized as follows:

1. Comparisons of data obtained by the new phase-change coating method with conventional thermocouple-calorimeter data showed relatively good agreement. The detail obtained in interference regions indicates that this method is very useful for obtaining heat-transfer data on complex shapes.

2. The presence of shear pads caused increases in heat transfer to the face in the vicinity of the pads by a factor of about 2 for a free-stream Reynolds number based on face diameter of 0.20×10^6.

3. Increasing the Reynolds number caused a larger area in the vicinity of the pads to be affected and may possibly have caused higher interference heating rates.

4. A small region of very high heat-transfer rate was found immediately ahead of the umbilical fairing on the leeward corner of the face. The increase in heating rate in this region may have been 8 to 10 times that of a smooth body.

5. The peak heat-transfer rate in the vicinity of the antenna on the windward afterbody was about 6 times the value for a smooth configuration.

6. The peak heat-transfer rate at the windward corner was about 1.5 times the stagnation-point value.

7. There were no large effects of afterbody cavities on the heat-transfer rates in the separated portion of the afterbody. However, because of the sting interference effects, the heating may be entirely different in the separated afterbody region of a free-flight vehicle.

8. Interference from the reaction-control jets caused increased heating rates over a large portion of the afterbody surface with the single exception of the pitch jet which had no noticeable effect. The maximum increases in heating rate caused by this interference were factors of 4 for the yaw jet, 11 for the forward-firing roll jet, and 3 for the aft-firing roll jet.

Langley Research Center,
    National Aeronautics and Space Administration,
        Langley Station, Hampton, Va., October 12, 1964.

1. Jones, Robert A.; and Hunt, James L.: Use of Temperature-Sensitive Coatings
   for Obtaining Quantitative Aerodynamic Heat-Transfer Data. AIAA J.,
   vol. 2, no. 7, July 1964, pp. 1354-1356.

2. Kasanoff, D. R.; and Kimmel, E.: Recent Developments in Fusible Temperature
   Indicators. Temperature - Its Measurement and Control in Science and
   Industry, vol. 3, pt. 2, Reinhold Pub. Corp., c.1962, pp. 1005-1007.

3. Carslaw, H. S.; and Jaeger, J. C.: Conduction of Heat in Solids. Second
   ed., Oxford Univ. Press, Inc., 1959.

4. Swann, Robert T.; and Pittman, Claud M.: Numerical Analysis of the Transient
   Response of Advanced Thermal Protection Systems for Atmospheric Entry.
   NASA TN D-1370, 1962.

5. Jones, Robert A.: Measured Heat-Transfer and Pressure Distributions on the
   Apollo Face at a Mach Number of 8 and Estimates for Flight Conditions.
   NASA TM X-919, 1964.

6. Jones, Robert A.: Experimental Investigation of the Overall Pressure Dis-
   tribution, Flow Field, and Afterbody Heat-Transfer Distribution of an
   Apollo-Type Reentry Configuration at a Mach Number of 8. NASA TM X-813,
   1963.

r_s

r_a

r_n

35°

s

u_∞

35°

r_c

Side view

0.175 in.

0.019 in. on pad 1 and 2
0.038 in. on pad 3

0.01 in. diam.

0.06 in.

Detail of shear pads

r_n = 1.200 D
r_s = 0.0948 D
r_a = 0.0918 D
r_c = 0.050 D
D = 4.00 in.

Pad 1

1.505 in.

47° 15'

12° 45'

Pad 3

62° 45'

Pad 2

View normal to face

Figure 1.- Sketch of model 1.
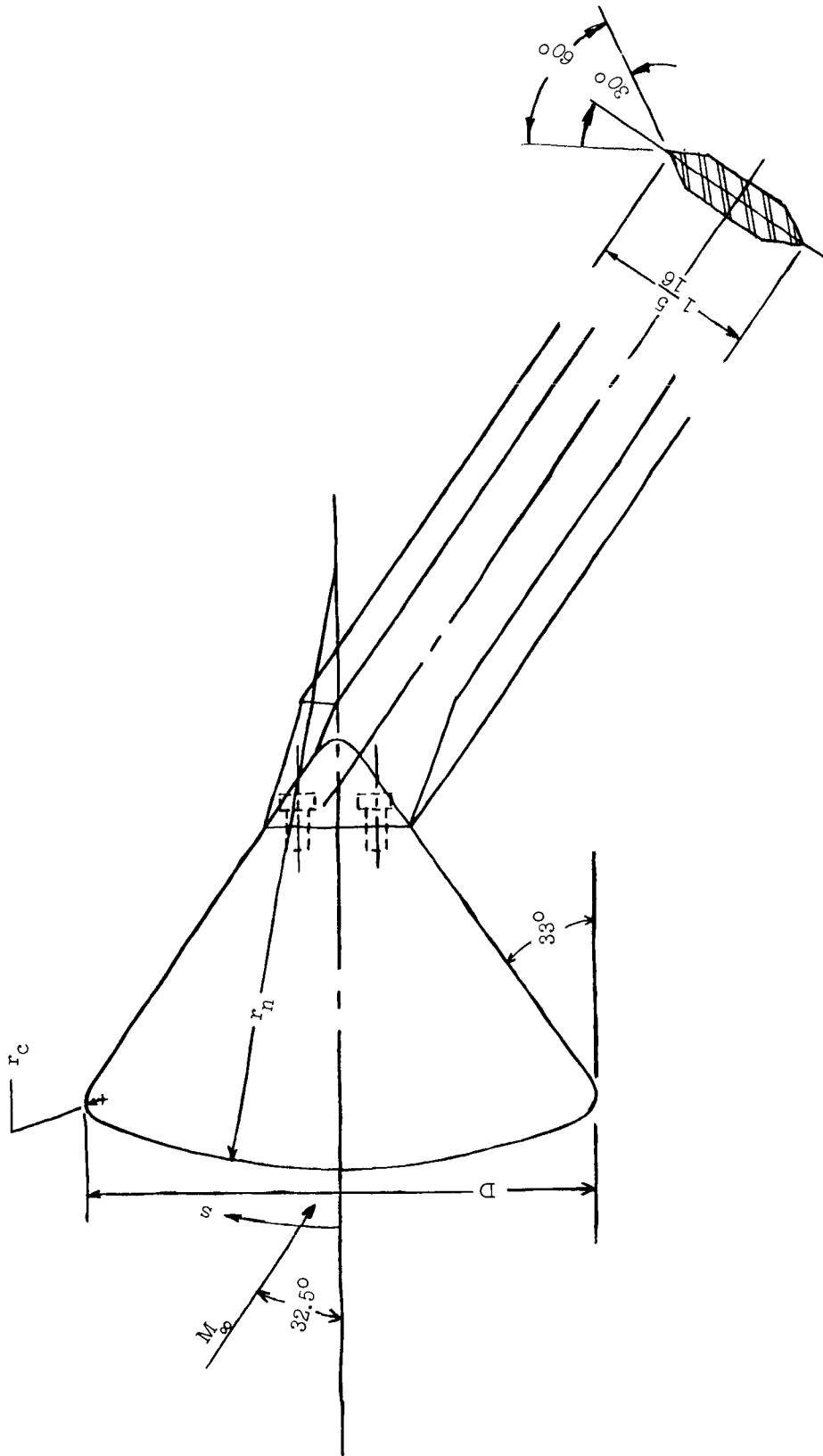
Figure 2.- Sketch of model 2.

Tension tie

Shear pad

Antenna

Umbilical fairing
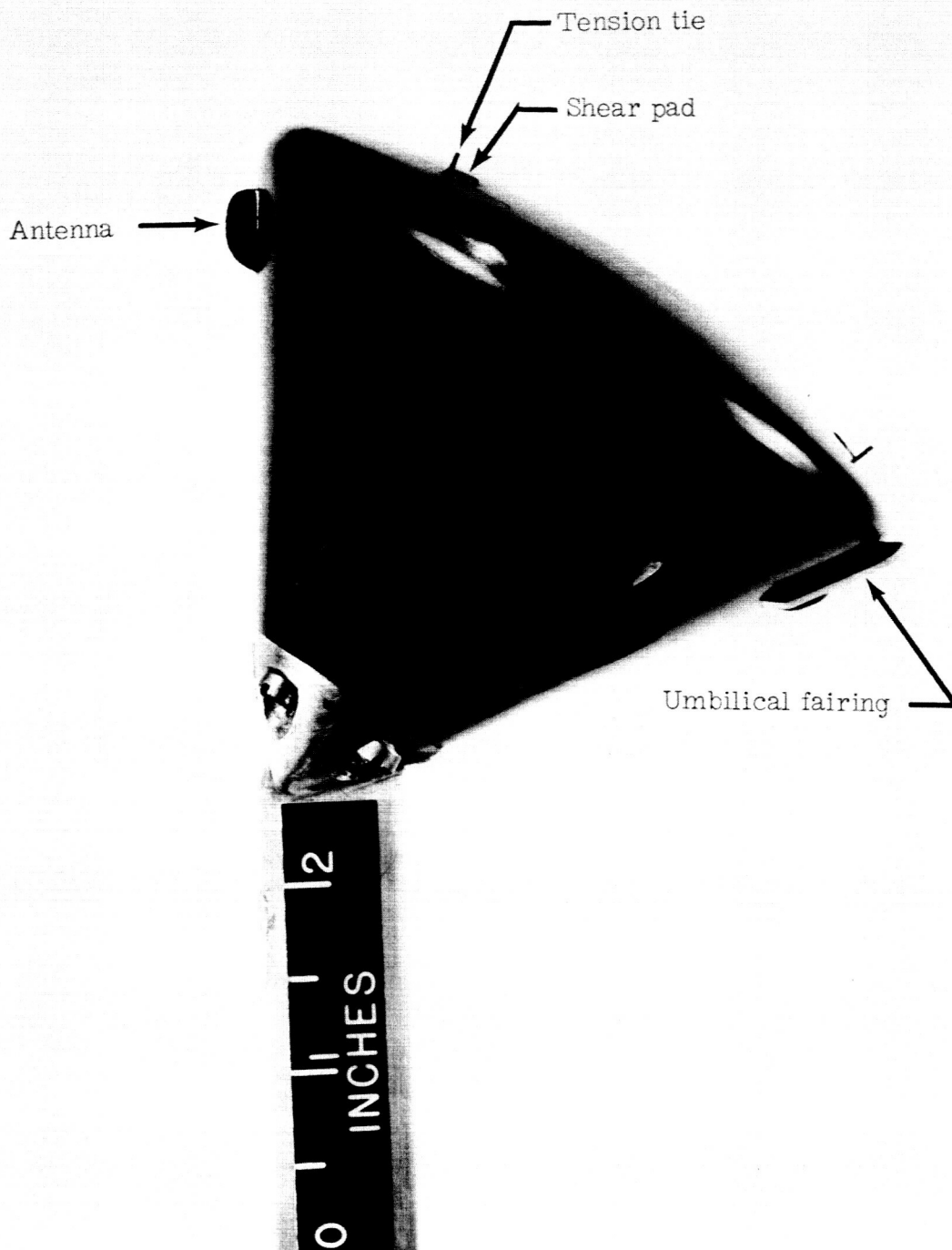
(a) Right side view.

L-64-2071.1

Figure 3.- Photographs of model 3.
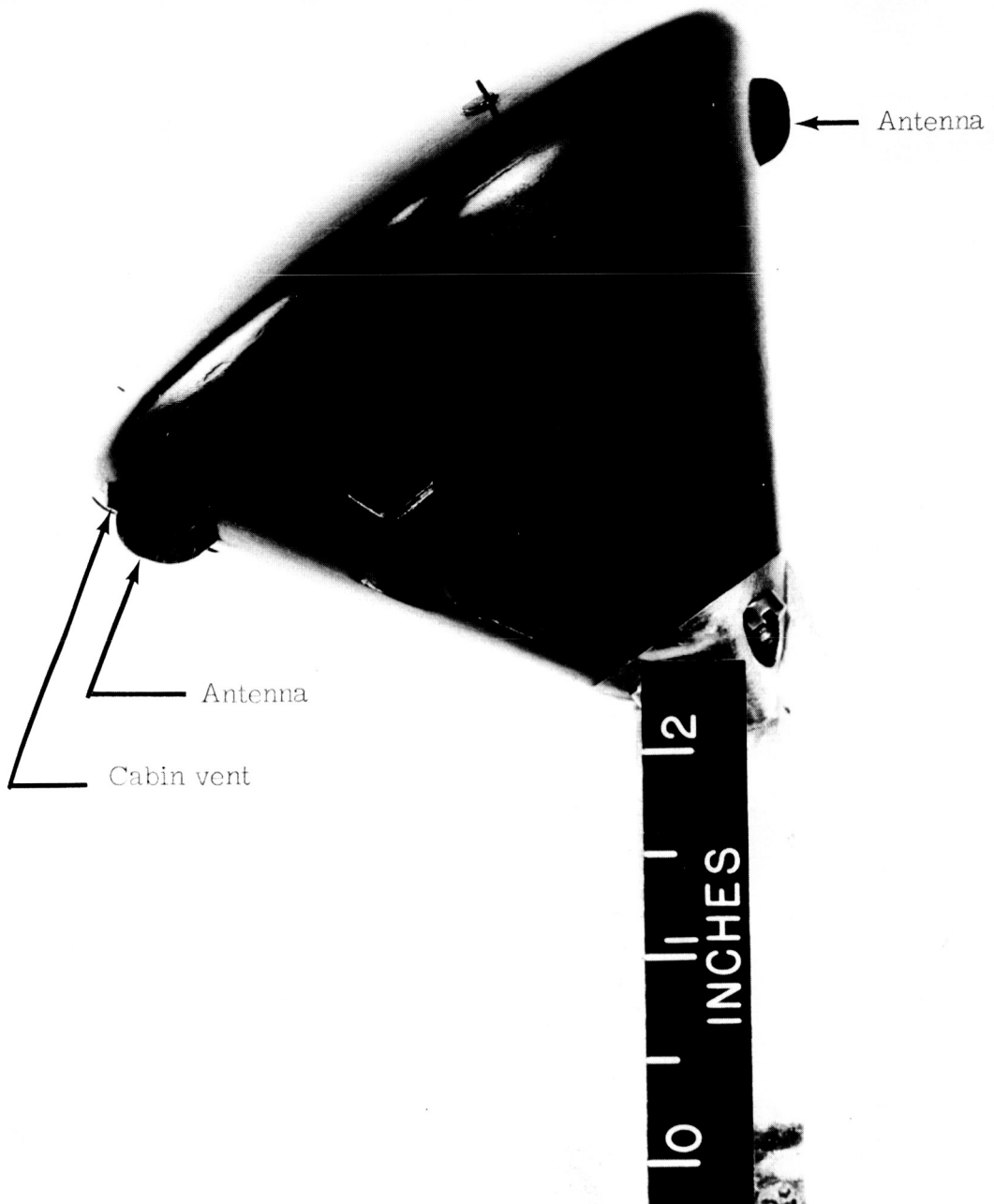
(b) Left side view.

L-64-2072.1

Figure 3.- Continued.

Shear pads

Umbilical fairing

Window

Window

Tower well

Cabin vent

Antenna

Window

Tower well

Crew hatch

INCHES
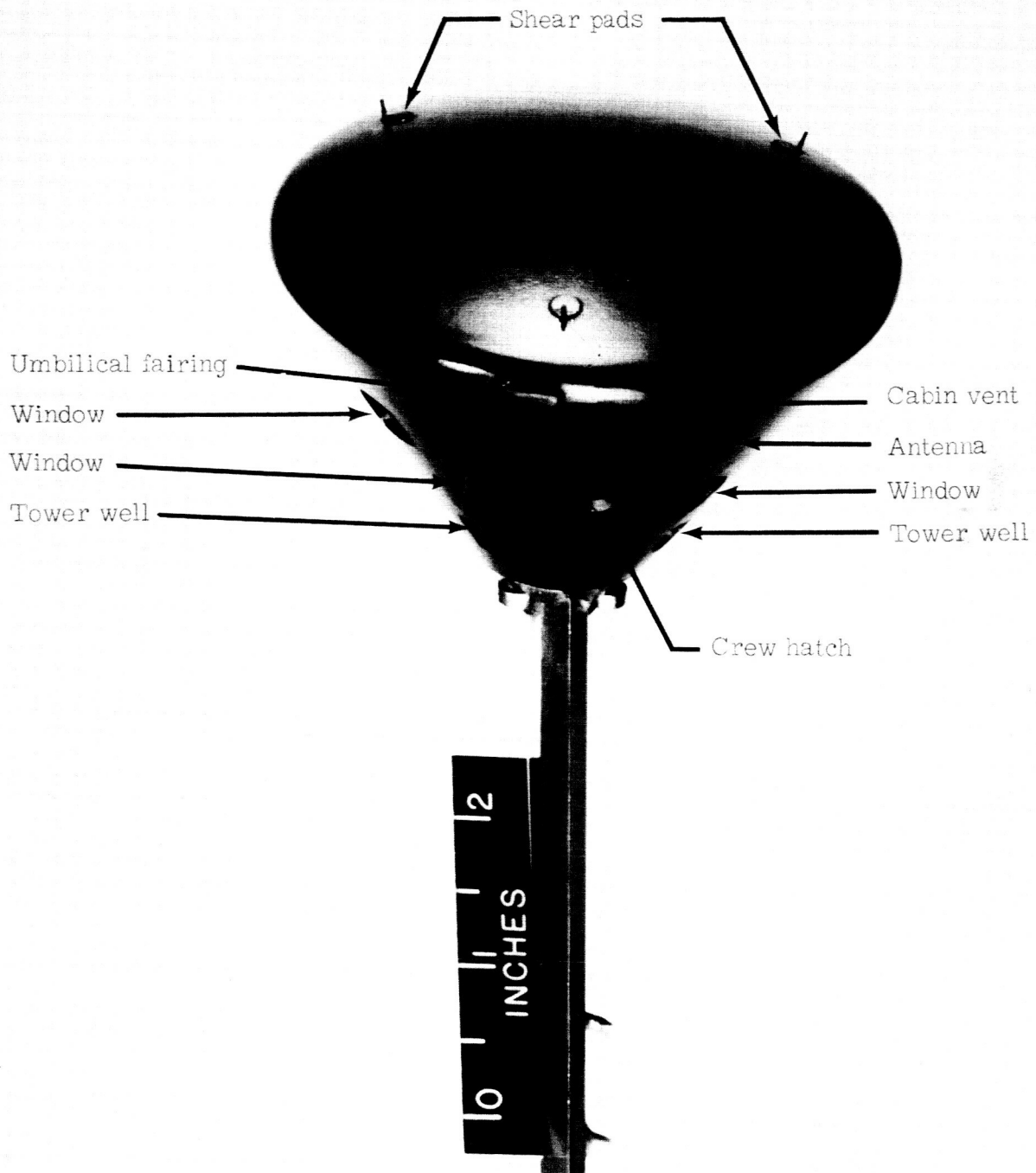
(c) Bottom view.

L-64-2070.1

Figure 3.- Continued.

Tension tie

Shear pad

Cabin vent

Umbilical fairing

Window

Window

Tower well

Window

Crew hatch

Window

Tower well

2

INCHES

0
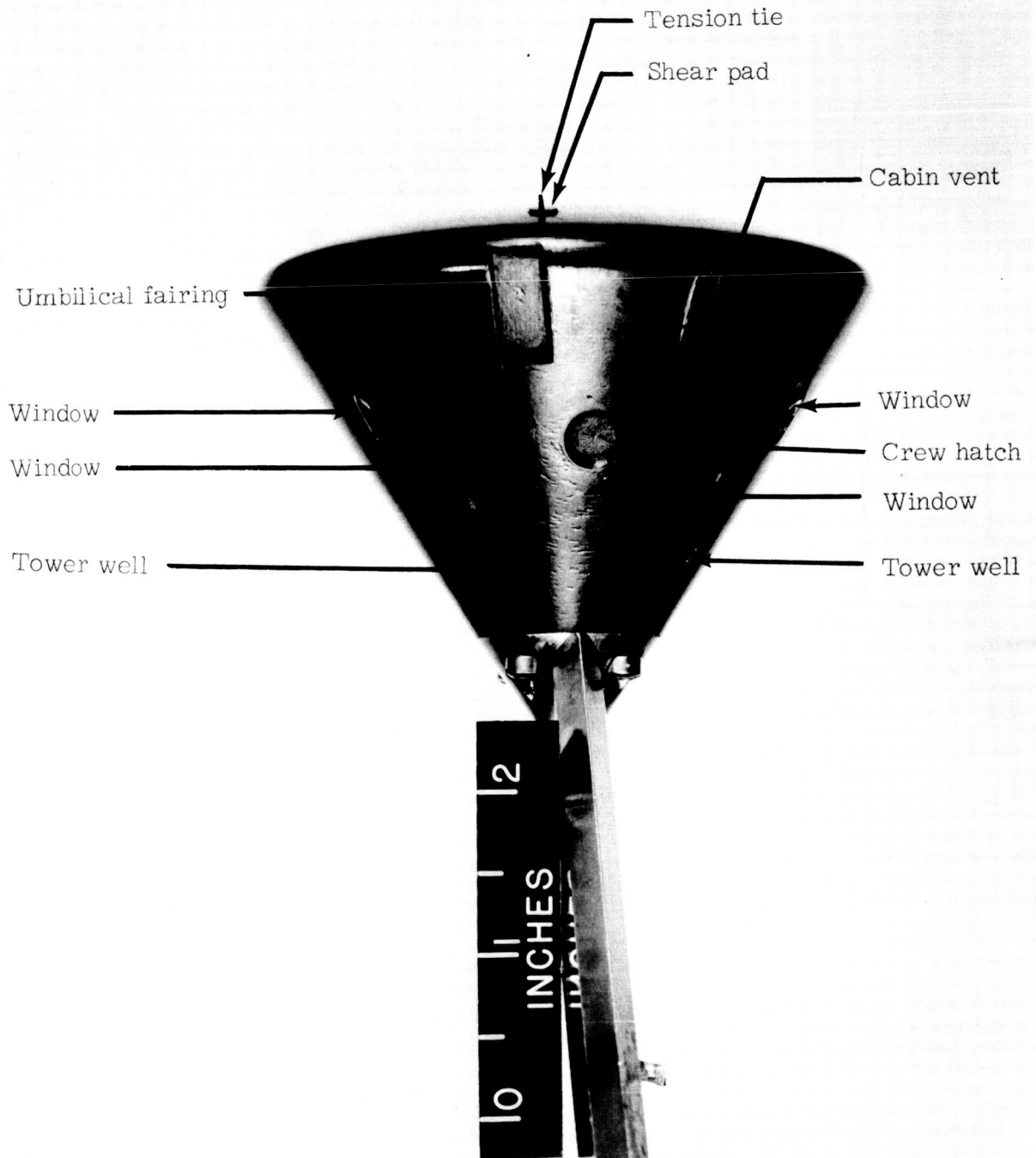
(d) Leeward afterbody view.

L-64-2073.1

Figure 3.- Concluded.

0.850 in.

1/4 in.

5°

0.873 in.

50°

1/16-inch layer
of plastic

42°45'

15°

58°

$1\frac{1}{2}°$

Hole 1

Hole 2
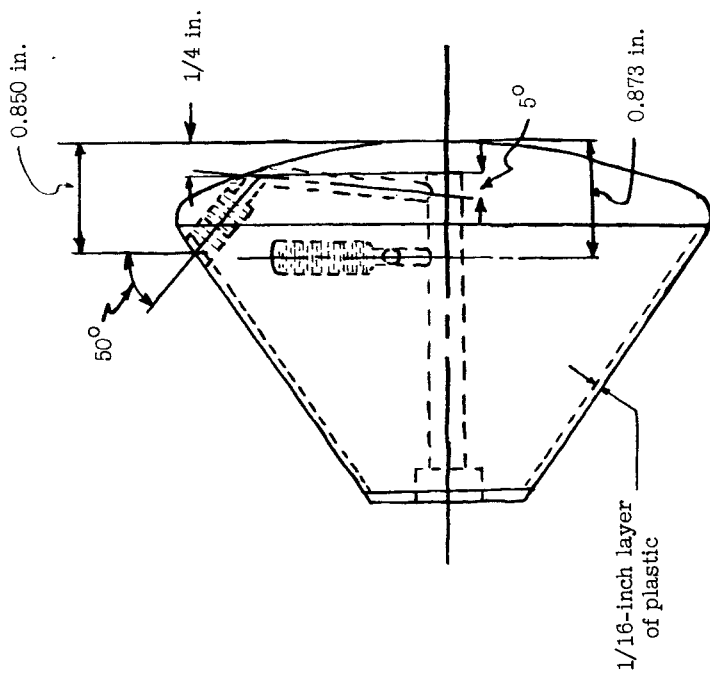
(a) Nozzle locations.

Figure 4.- Sketch of model 4.
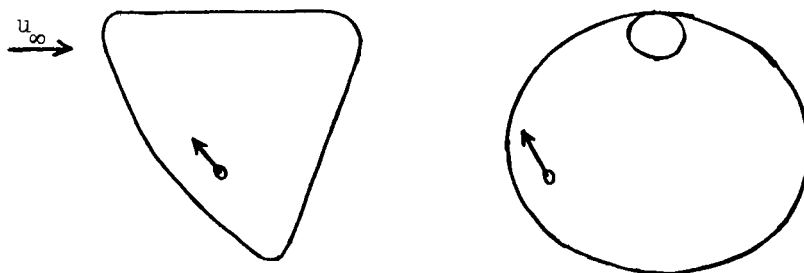
Forward-firing roll jet
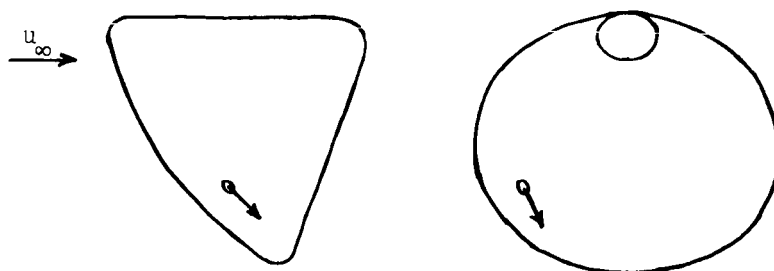
Aft-firing roll jet
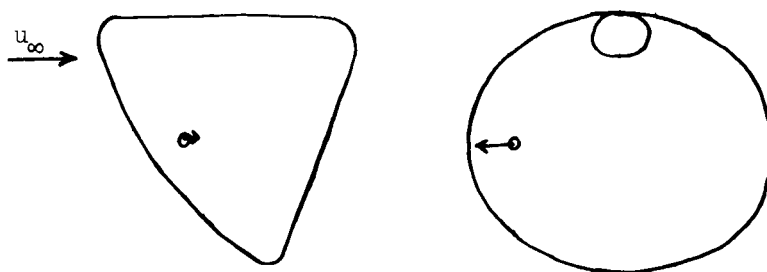
Yaw jet
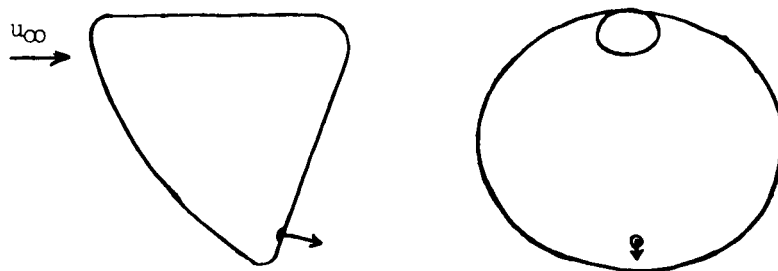
Pitch jet

(b) Sketch showing thrust vectors of jets.

Figure 4.- Concluded.

Increasing time
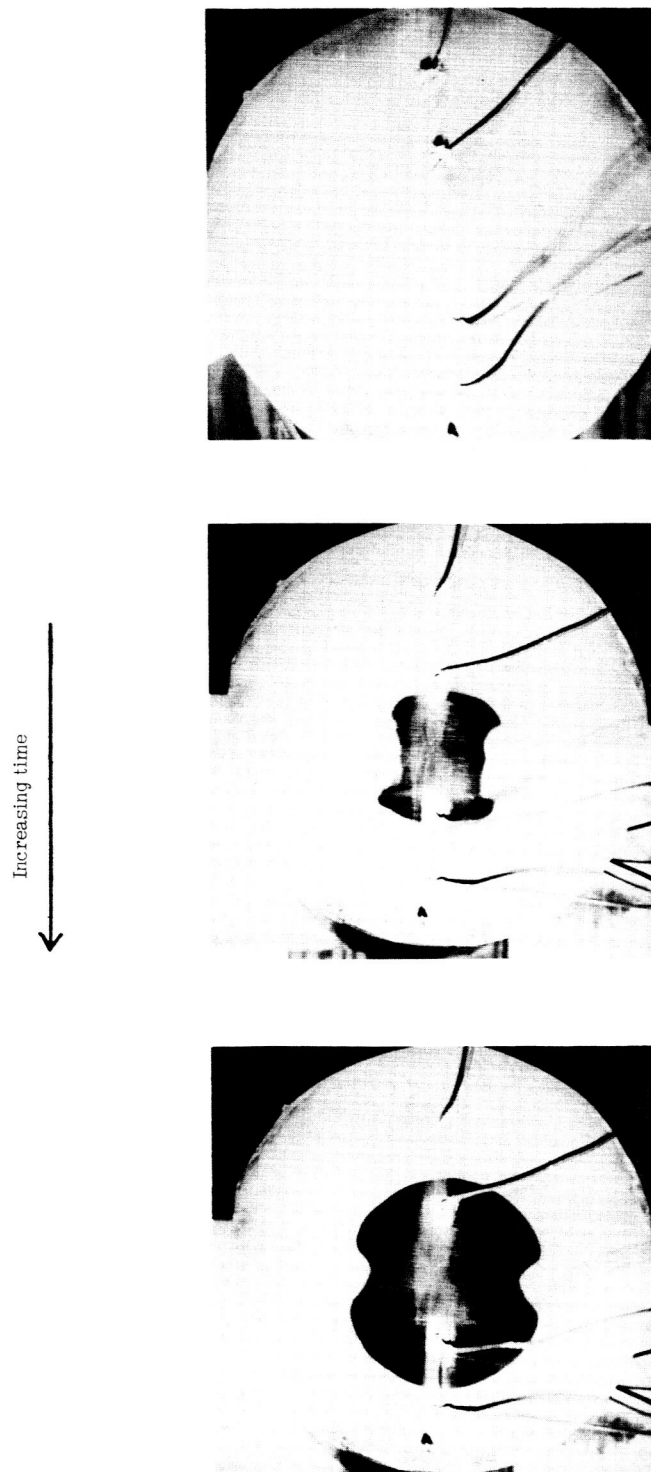
L-64-8369
Figure 5.- Photographs of phase-change patterns in calibration apparatus.
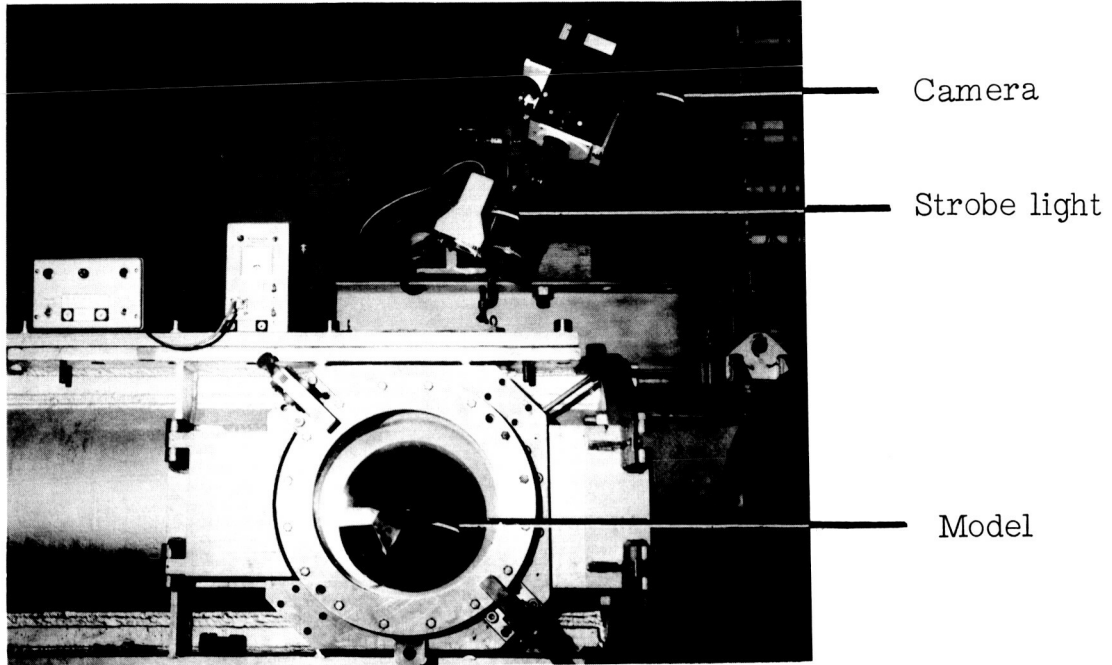
Figure 6.- Photograph of test setup.   L-64-8370
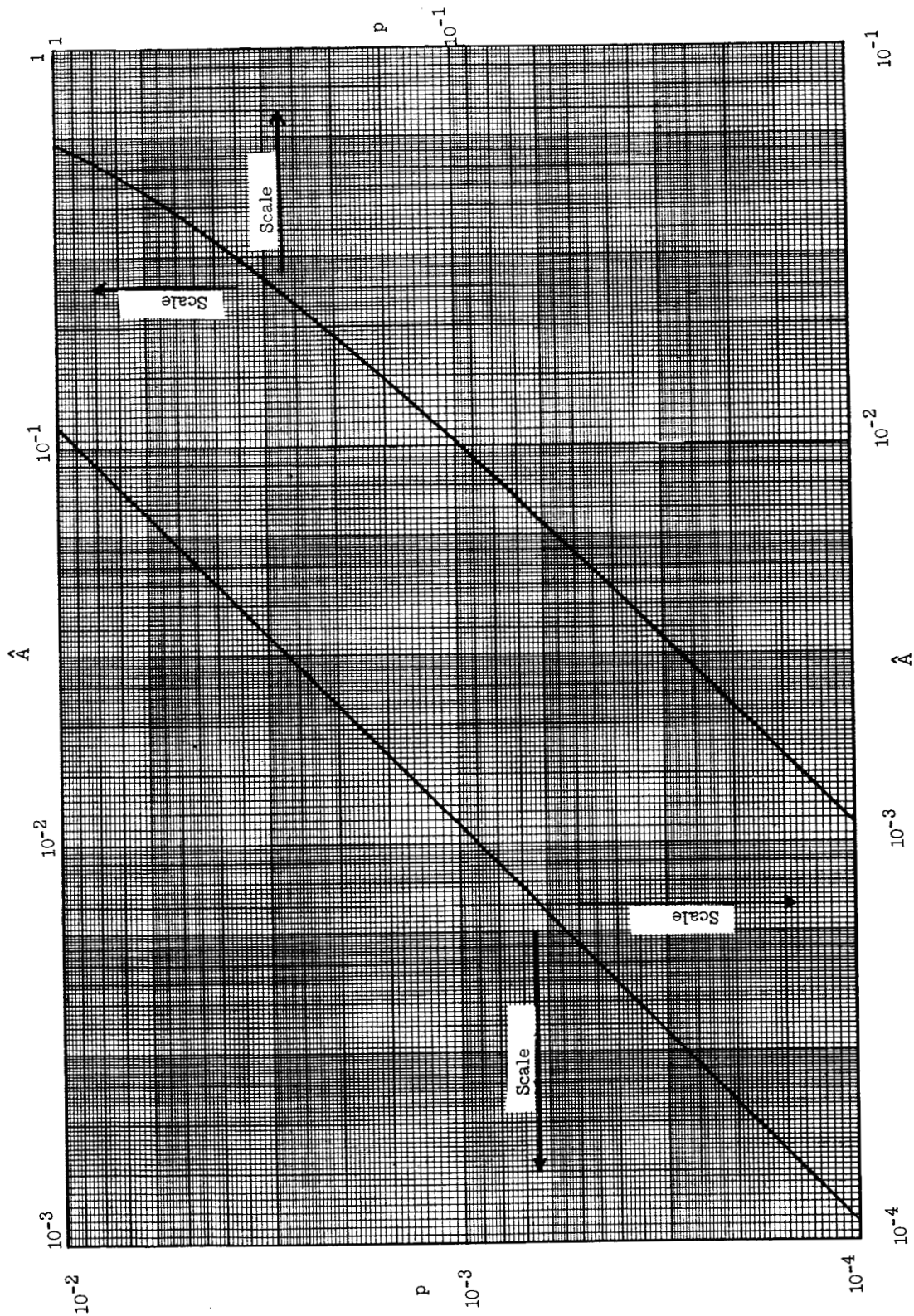
Figure 7.- Solution of heat conduction equation (eq. (5)).

$$A = \frac{A - T_i}{T_{aw} - T_i}$$

0.500
0.400
0.300
0.200
0.100
0.070
0.040
0.020
0.010
0.007
0.004
0.002
0.001

Time, sec

100
10
1
.1
.01

.001 .01 .1 1.0

$\frac{h}{k}\sqrt{\alpha}$
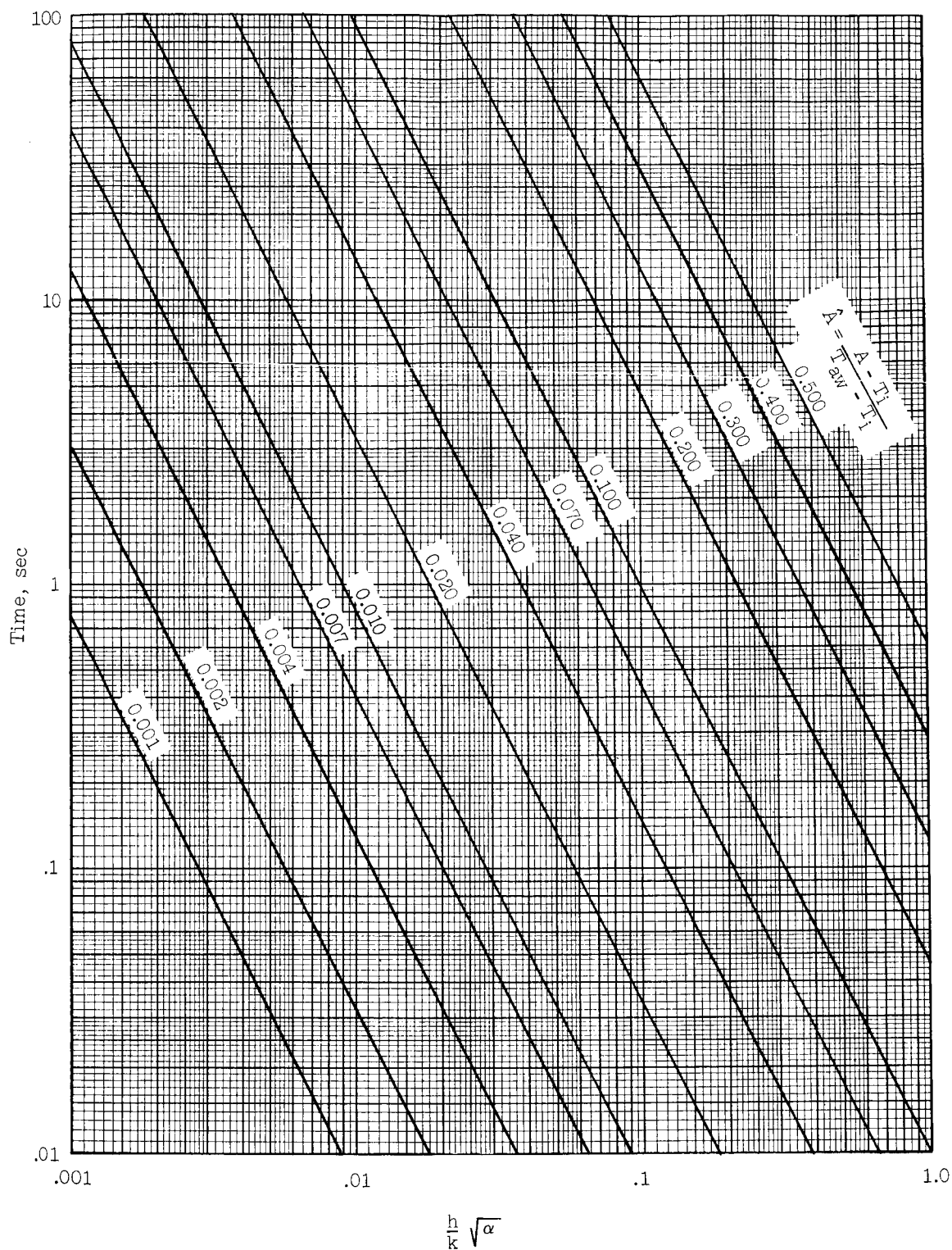
Figure 8.- Alternate plot of solution of heat conduction equation (eq. (5)).
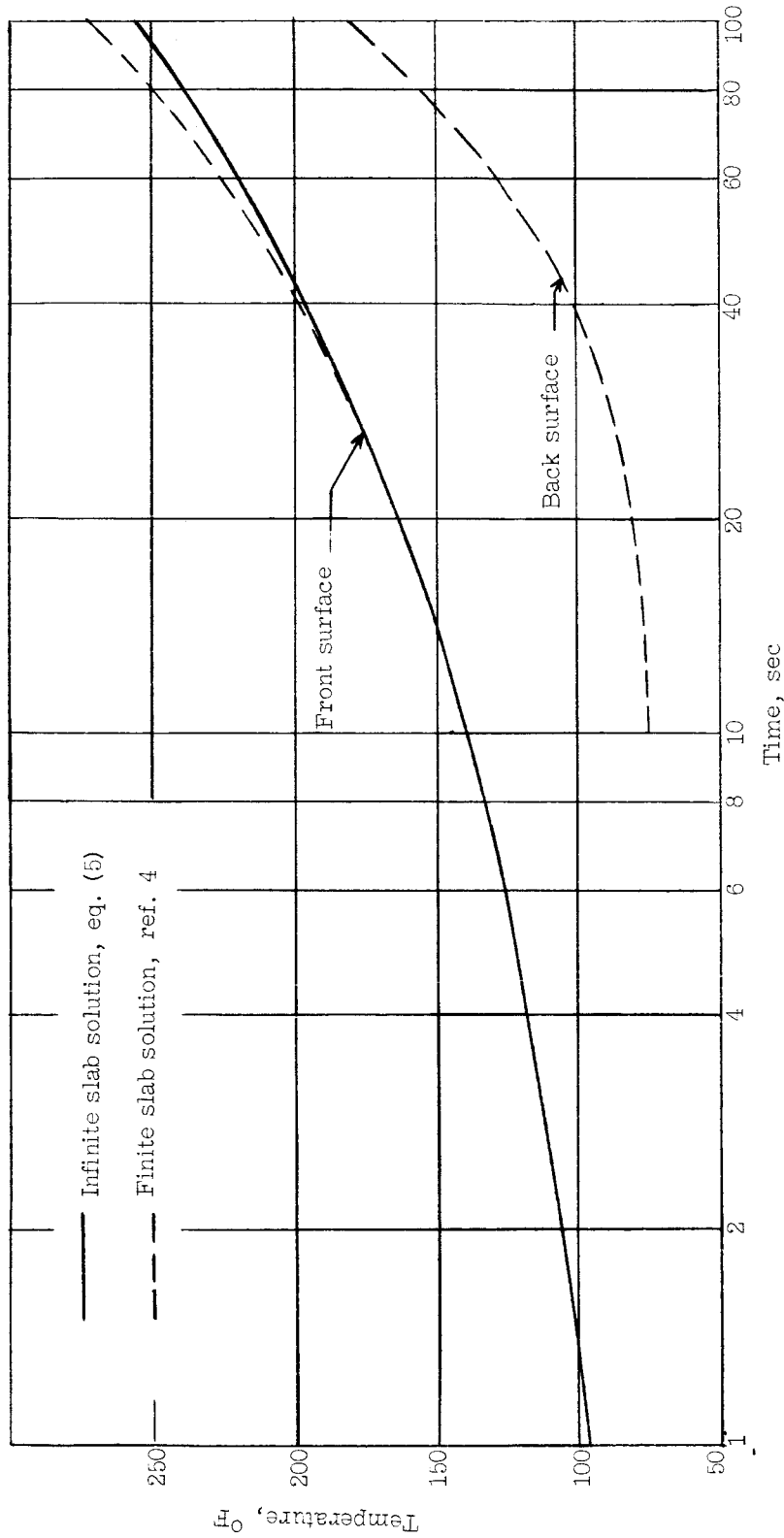
Figure 9.- Effect of finite slab on surface temperature.
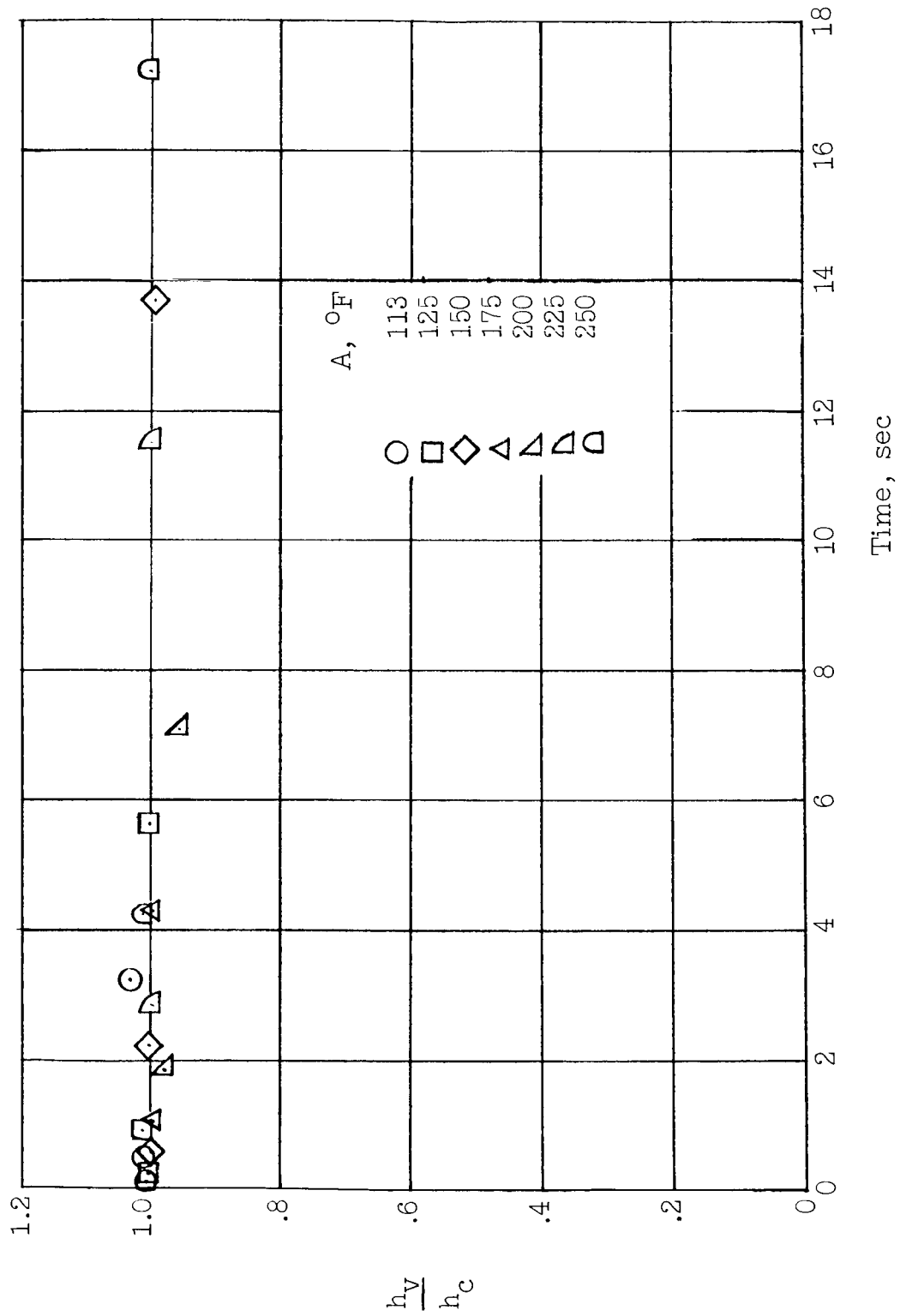
Figure 10.- Effect of temperature-dependent material properties on heat-transfer coefficients.
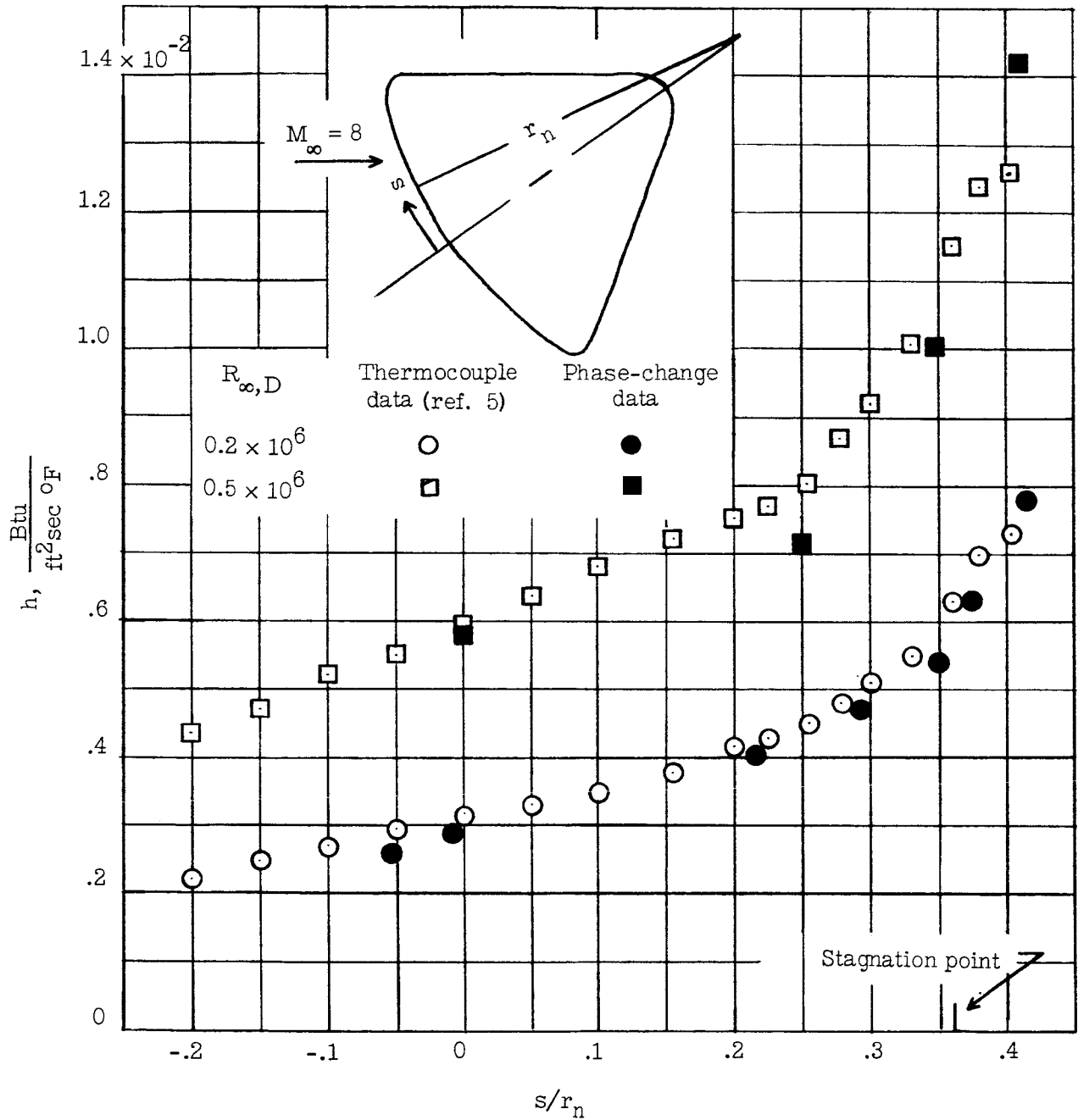
Figure 11.- Comparison of thermocouple-calorimeter and phase-change data for smooth face for vertical plane of symmetry.
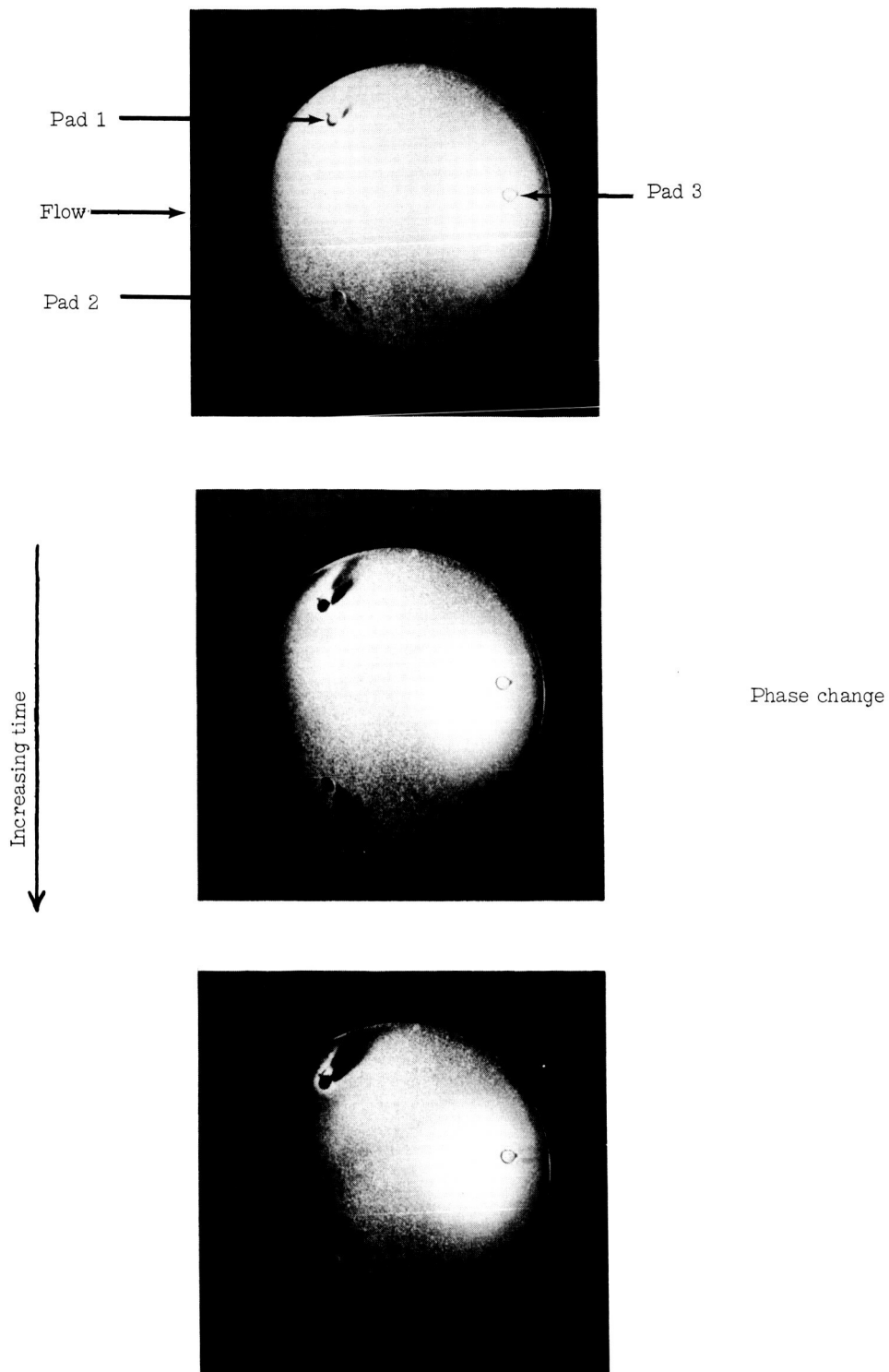
Figure 12.- Photographs of phase-change patterns.   Model 1; $R_{\infty,D} = 0.2 \times 10^6$.
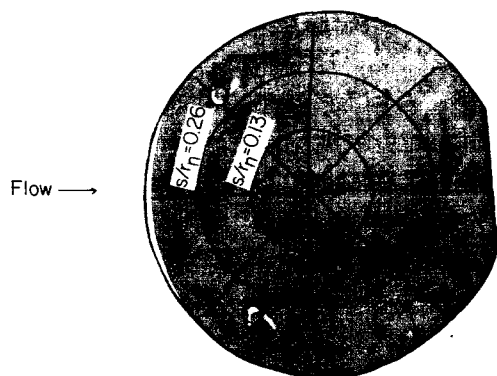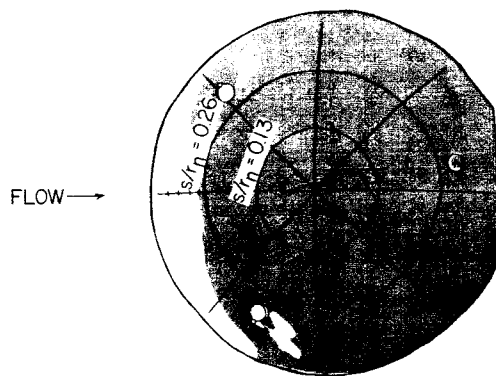
L-64-8371

Flow ⟶

(a) $h = 7.6 \times 10^{-3}$; $\frac{h}{h_o} = 1.17$.

(b) $h = 7.2 \times 10^{-3}$; $\frac{h}{h_o} = 1.11$.

(c) $h = 6.4 \times 10^{-3}$; $\frac{h}{h_o} = 1.0$.
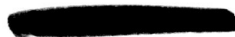
FLOW ⟶

(d) $h = 4.9 \times 10^{-3}$; $\frac{h}{h_o} = 0.75$.
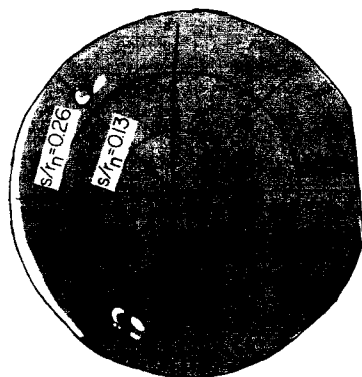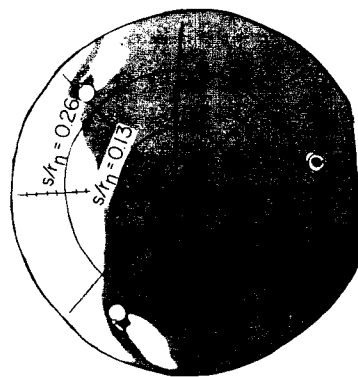
(e) $h = 3.8 \times 10^{-3}$; $\frac{h}{h_o} = 0.58$.
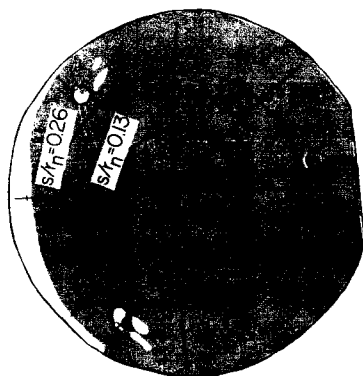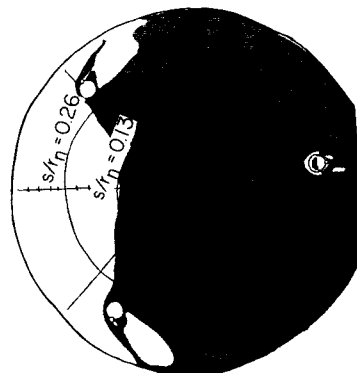
(f) $h = 3.4 \times 10^{-3}$; $\frac{h}{h_o} = 0.54$.

Figure 13.- Heat-transfer patterns on face. Model 1; $R_{\infty,D} = 0.2 \times 10^6$; $A = 150^\circ$ F.

FLOW—
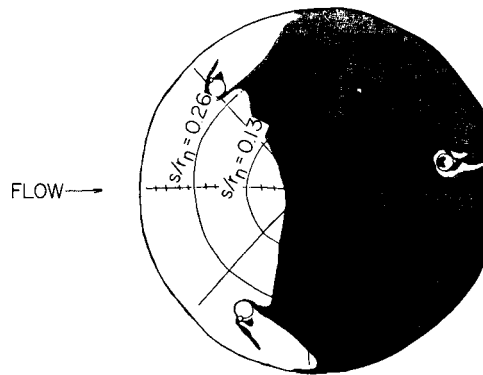
(g) $h = 3.2 \times 10^{-3}$; $\frac{h}{h_o} = 0.51$.
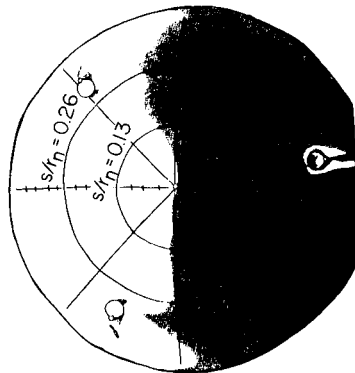
(h) $h = 3.0 \times 10^{-3}$; $\frac{h}{h_o} = 0.47$.
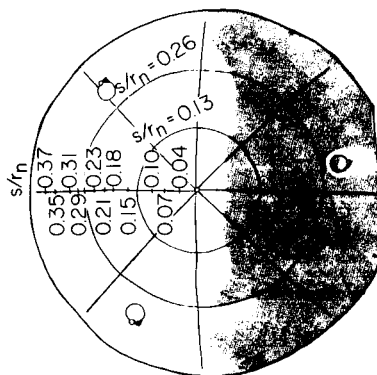
(i) $h = 2.7 \times 10^{-3}$; $\frac{h}{h_o} = 0.42$.

Figure 13.- Concluded.

Flow ⟶
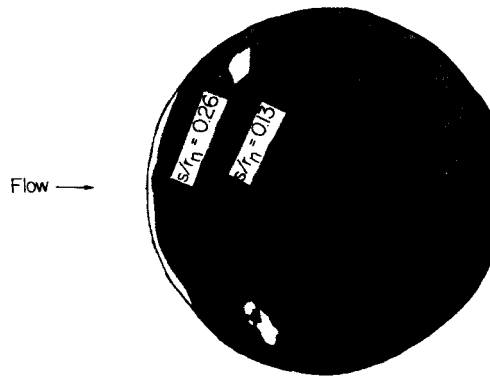
(a) $h = 1.39 \times 10^{-2}$; $\frac{h}{h_0} = 1.2$.
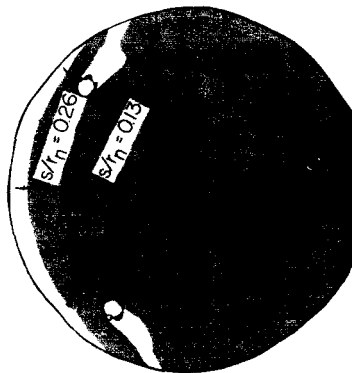
(b) $h = 1.15 \times 10^{-2}$; $\frac{h}{h_0} = 1.0$.
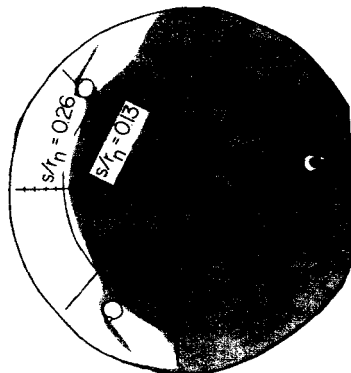
(c) $h = 0.75 \times 10^{-2}$; $\frac{h}{h_0} = 0.65$.

Figure 14.- Heat-transfer patterns on face. Model 1; $R_{\infty,D} = 0.5 \times 10^6$; $A = 175^\circ$ F.
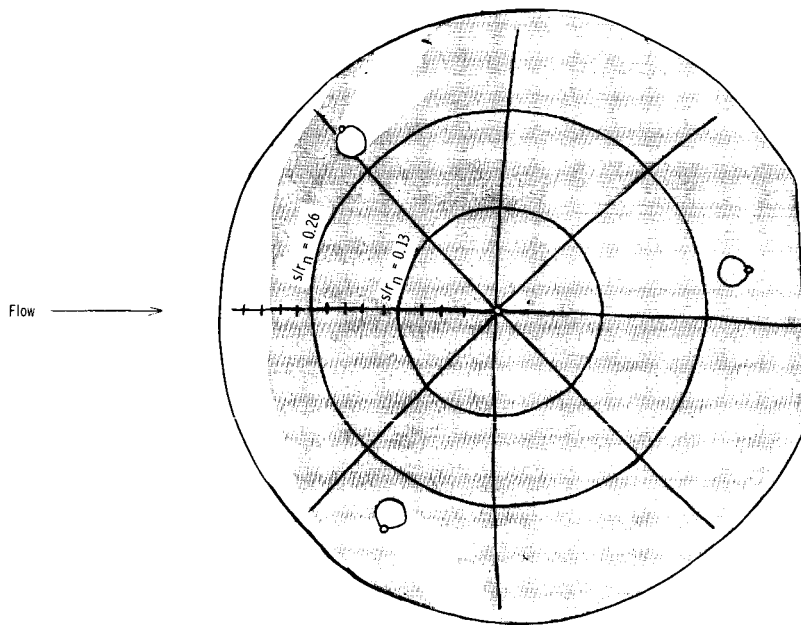
(a) $h = 1.8 \times 10^{-2}$; $\frac{h}{h_0} = 0.84$.
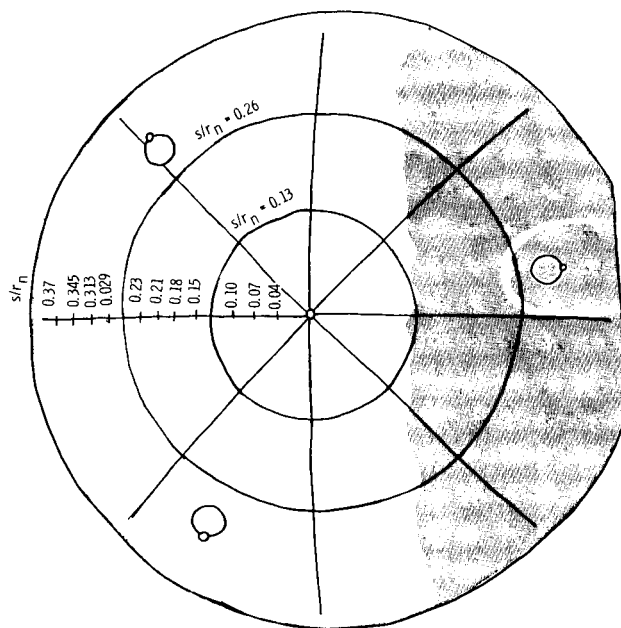
(b) $h = 0.8 \times 10^{-2}$; $\frac{h}{h_0} = 0.37$.

Figure 15.- Heat-transfer rates on face. Model 1; $R_{\infty,D} = 1.5 \times 10^6$; $A = 250^0$ F.

Flow →

Increasing time →
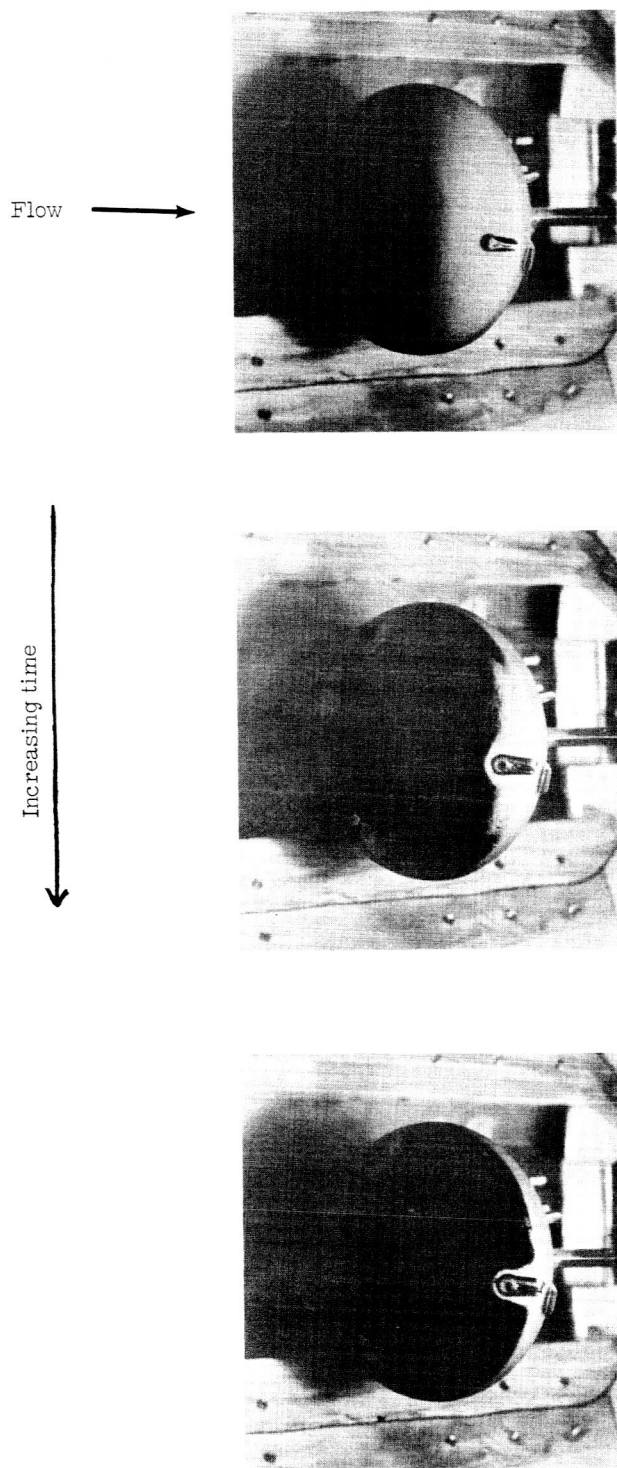
L-64-8372

Figure 16.- Photographs of phase-change patterns on face. Model 3; $R_{\infty,D} = 0.5 \times 10^6$.
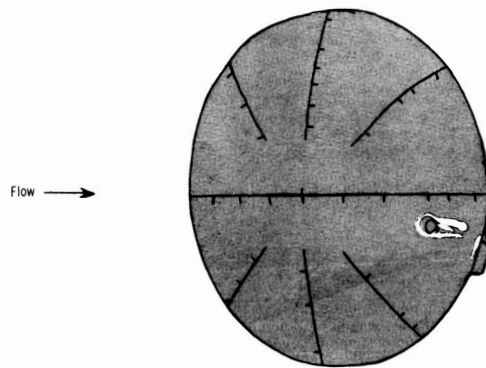
(a) $h = 8.23 \times 10^{-3}$; $\frac{h}{h_o} = 0.87$.
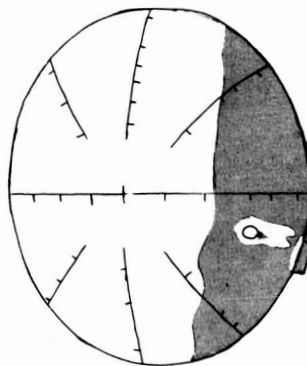
(b) $h = 5.55 \times 10^{-3}$; $\frac{h}{h_o} = 0.49$.
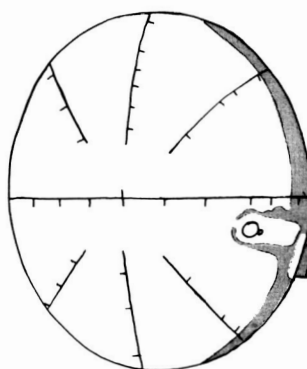
(c) $h = 3.76 \times 10^{-3}$; $\frac{h}{h_o} = 0.33$.

Figure 17.- Heat-transfer patterns on face.   Model 3; $R_{\infty,D} = 0.5 \times 10^6$.

Flow $\longrightarrow$
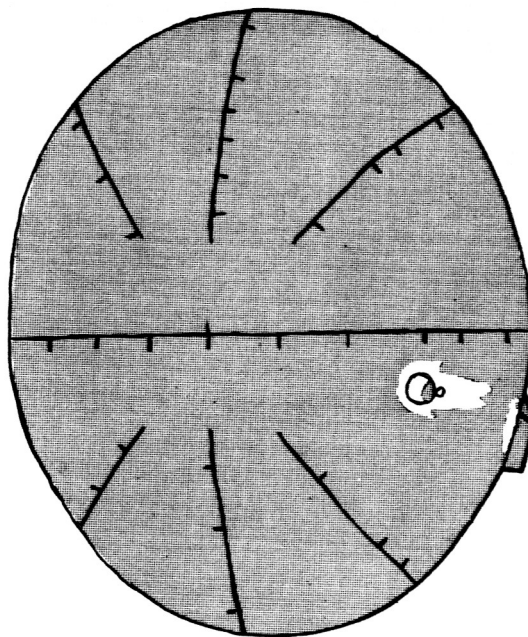
(a) $h = 1.70 \times 10^{-2}$; $\dfrac{h}{h_0} = 0.90$.
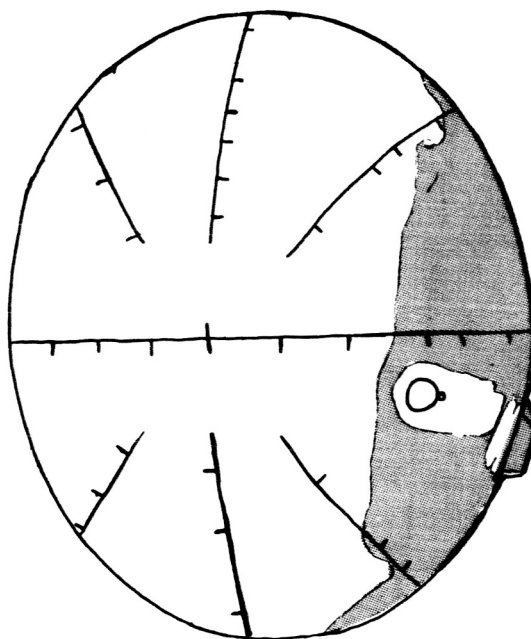
(b) $h = 0.80 \times 10^{-2}$; $\dfrac{h}{h_0} = 0.42$.

Figure 18.- Heat-transfer patterns on face.   Model 3; $R_{\infty,D} = 1.4 \times 10^6$.
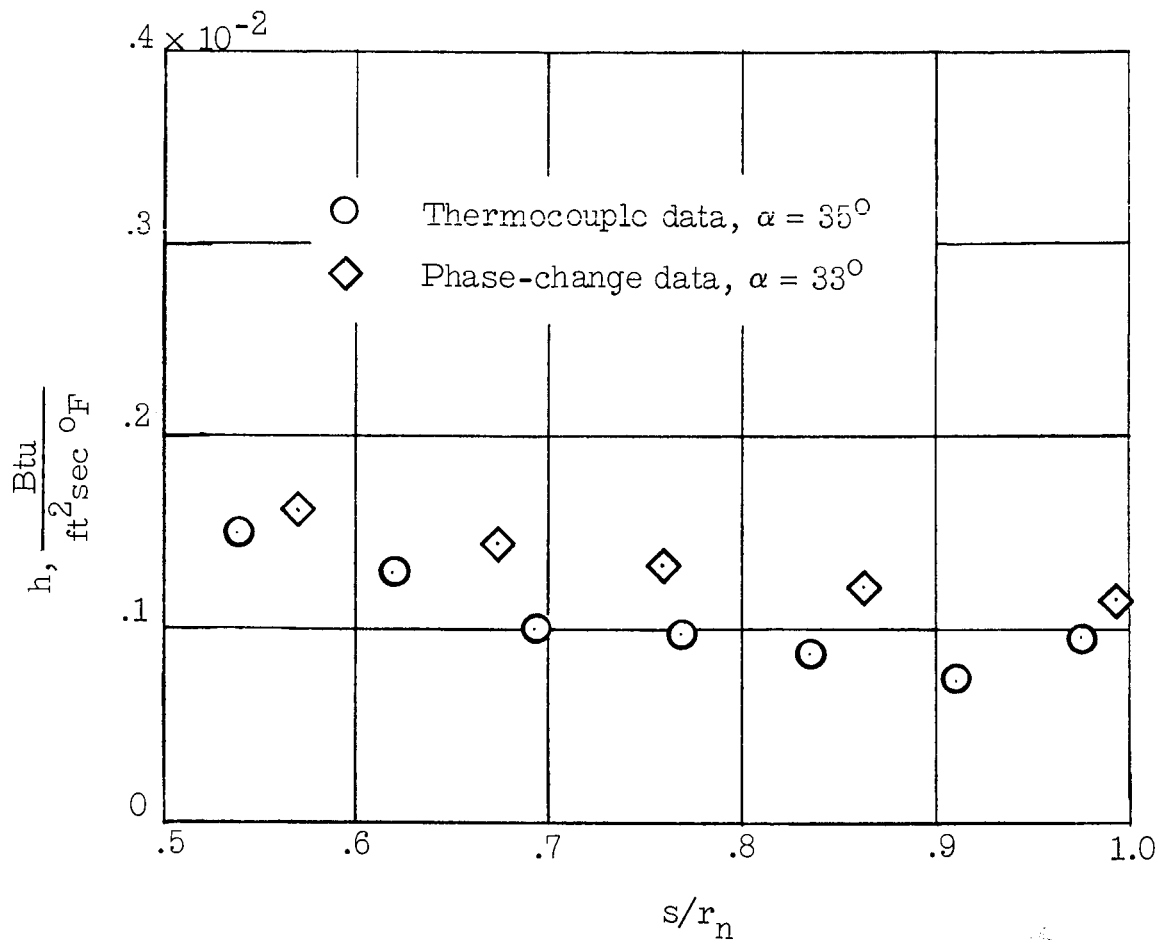
Figure 19.- Comparison of thermocouple-calorimeter and phase-change data along windward ray of afterbody. $R_{\infty,D} = 0.5 \times 10^6$.

Flow ⟶

Flow ⟶

(a) $h = 1.63 \times 10^{-3}$; $\dfrac{h}{h_0} = 0.18$.

(d) $h = 1.23 \times 10^{-3}$; $\dfrac{h}{h_0} = 0.13$.

(b) $h = 1.46 \times 10^{-3}$; $\dfrac{h}{h_0} = 0.16$.

(e) $h = 1.15 \times 10^{-3}$; $\dfrac{h}{h_0} = 0.12$.

(c) $h = 1.33 \times 10^{-3}$; $\dfrac{h}{h_0} = 0.14$.

(f) $h = 1.03 \times 10^{-3}$; $\dfrac{h}{h_0} = 0.12$.
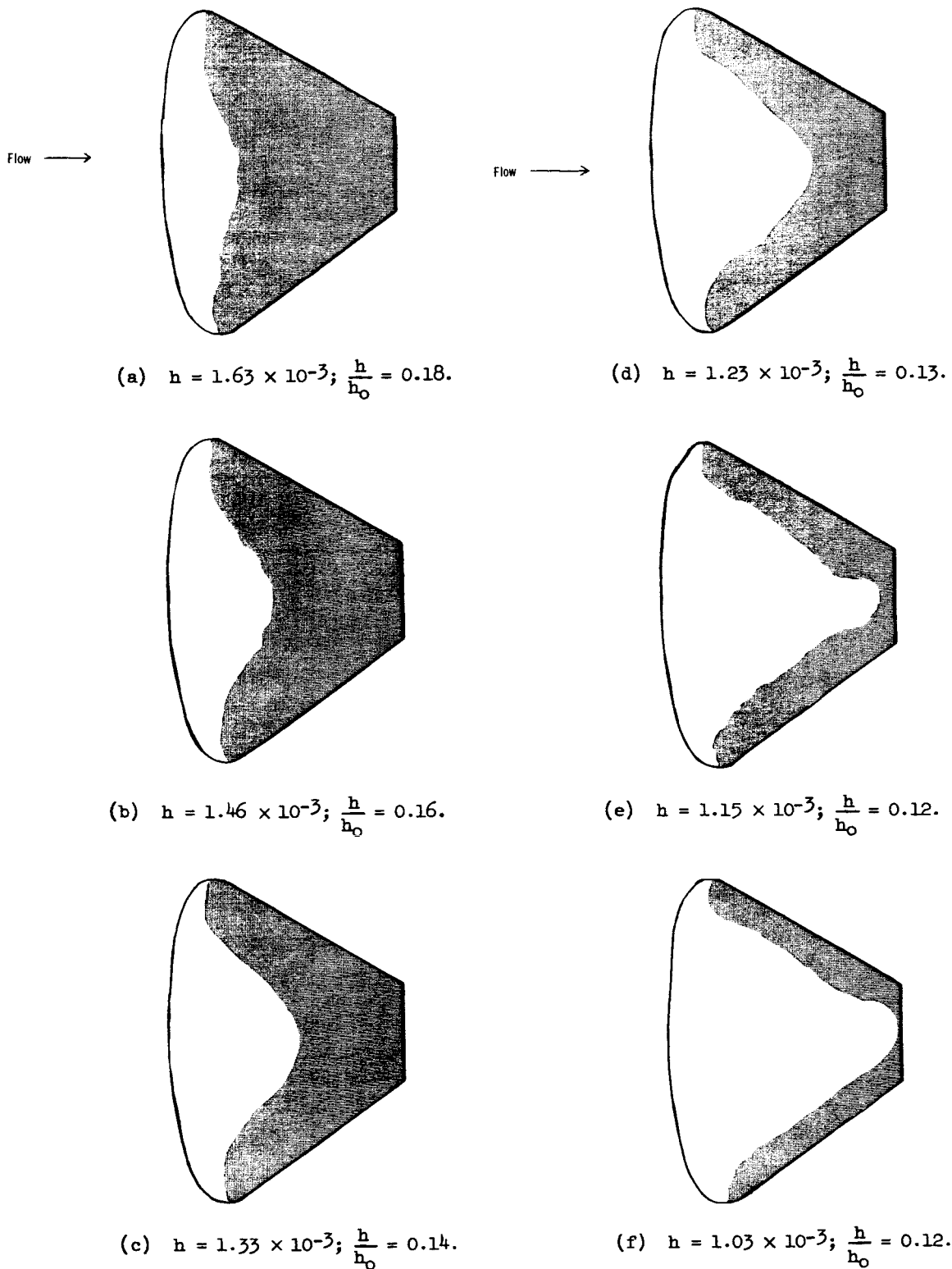
Figure 20.- Heat-transfer patterns on windward afterbody of smooth configuration viewed from top. $R_{\infty,D} = 0.5 \times 10^{6}$.

Flow

Tangent line

Portion of model
shown in figure 21
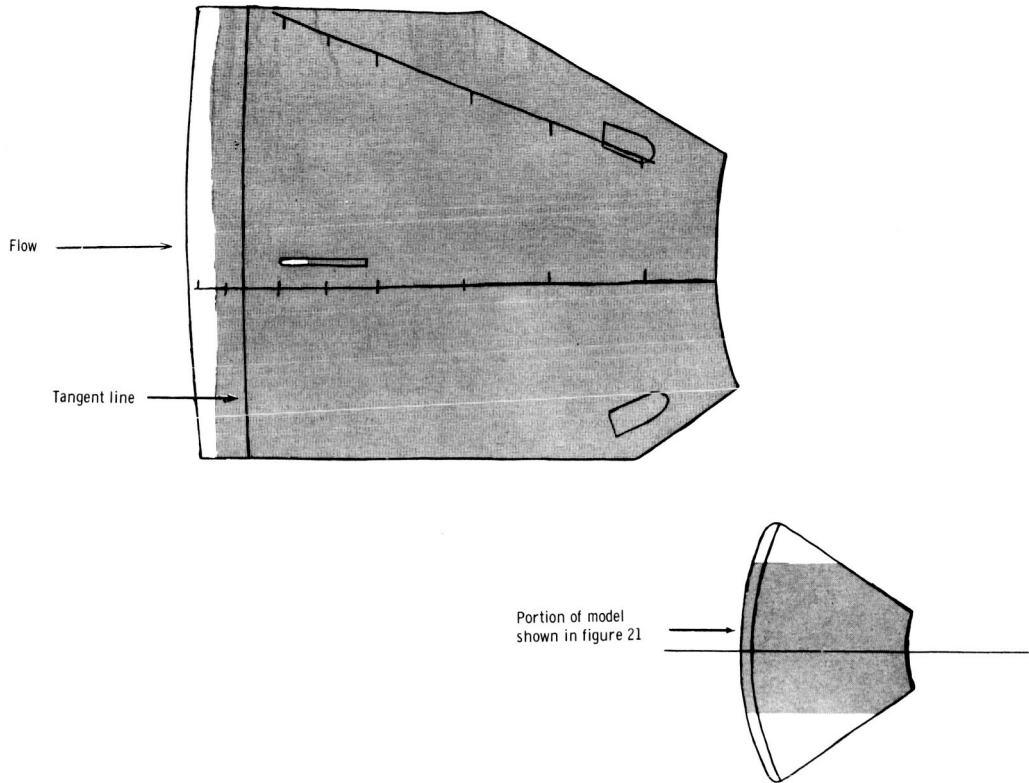
(a) $h = 1.45 \times 10^{-2}$; $\dfrac{h}{h_o} = 1.55$.
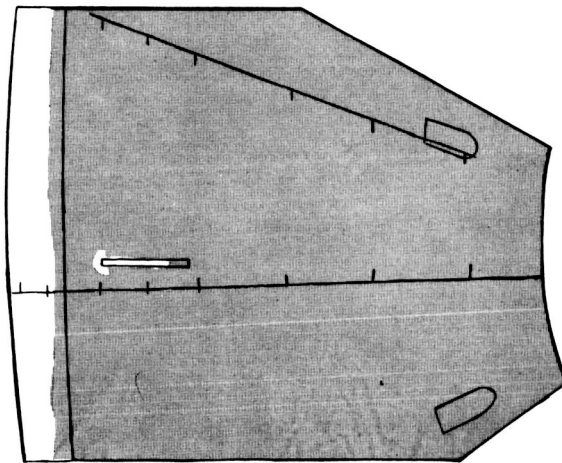
(b) $h = 9.91 \times 10^{-3}$; $\dfrac{h}{h_o} = 1.06$.

Figure 21.- Heat-transfer patterns on windward afterbody. Model 3; $R_{\infty,D} = 0.5 \times 10^6$.

Flow
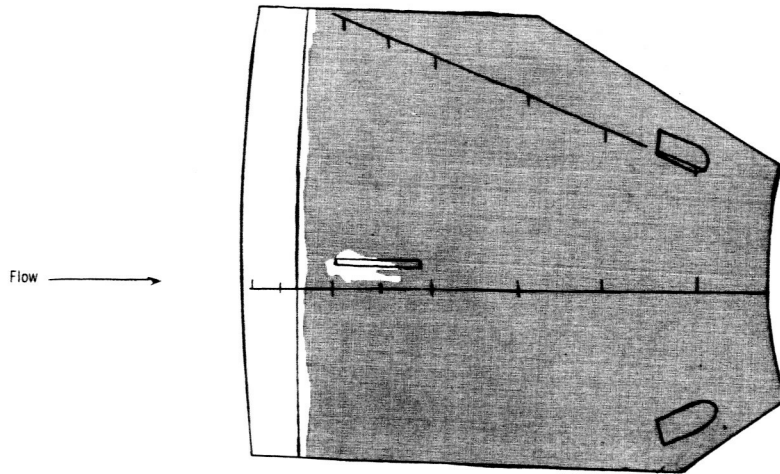
(c) $h = 5.59 \times 10^{-3}$; $\dfrac{h}{h_0} = 0.60$.
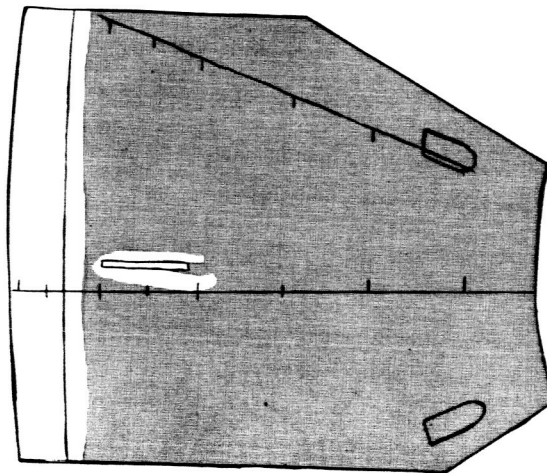
(d) $h = 3.54 \times 10^{-3}$; $\dfrac{h}{h_0} = 0.38$.

Figure 21.- Continued.

Flow ⟶

(e) $h = 2.05 \times 10^{-3}$; $\frac{h}{h_0} = 0.22$.

0.40 0.45 0.50 0.55 0.60 0.70 0.80 0.90
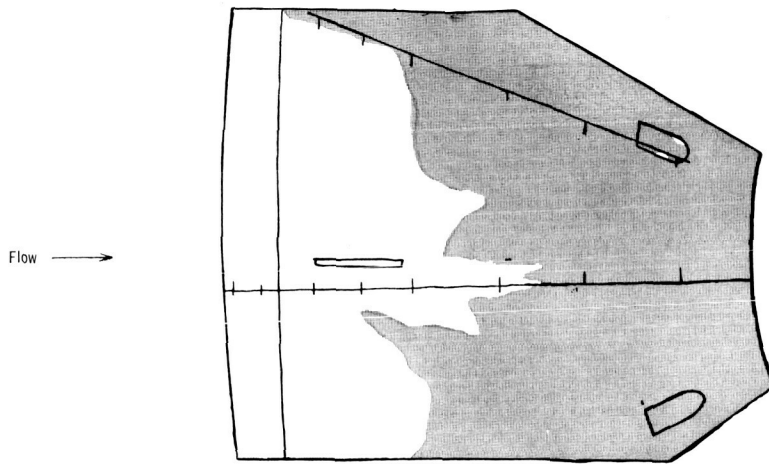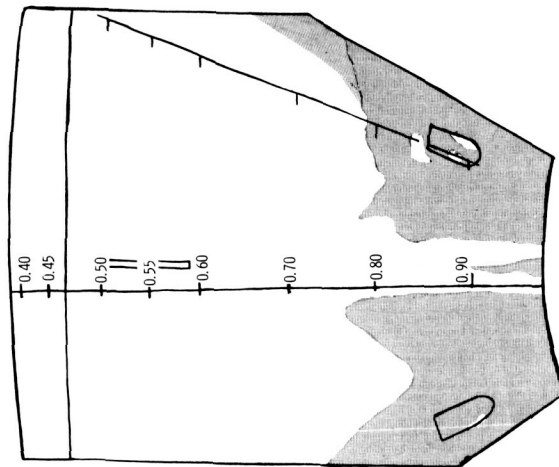
(f) $h = 1.52 \times 10^{-3}$; $\frac{h}{h_0} = 0.16$.

Figure 21.- Concluded.
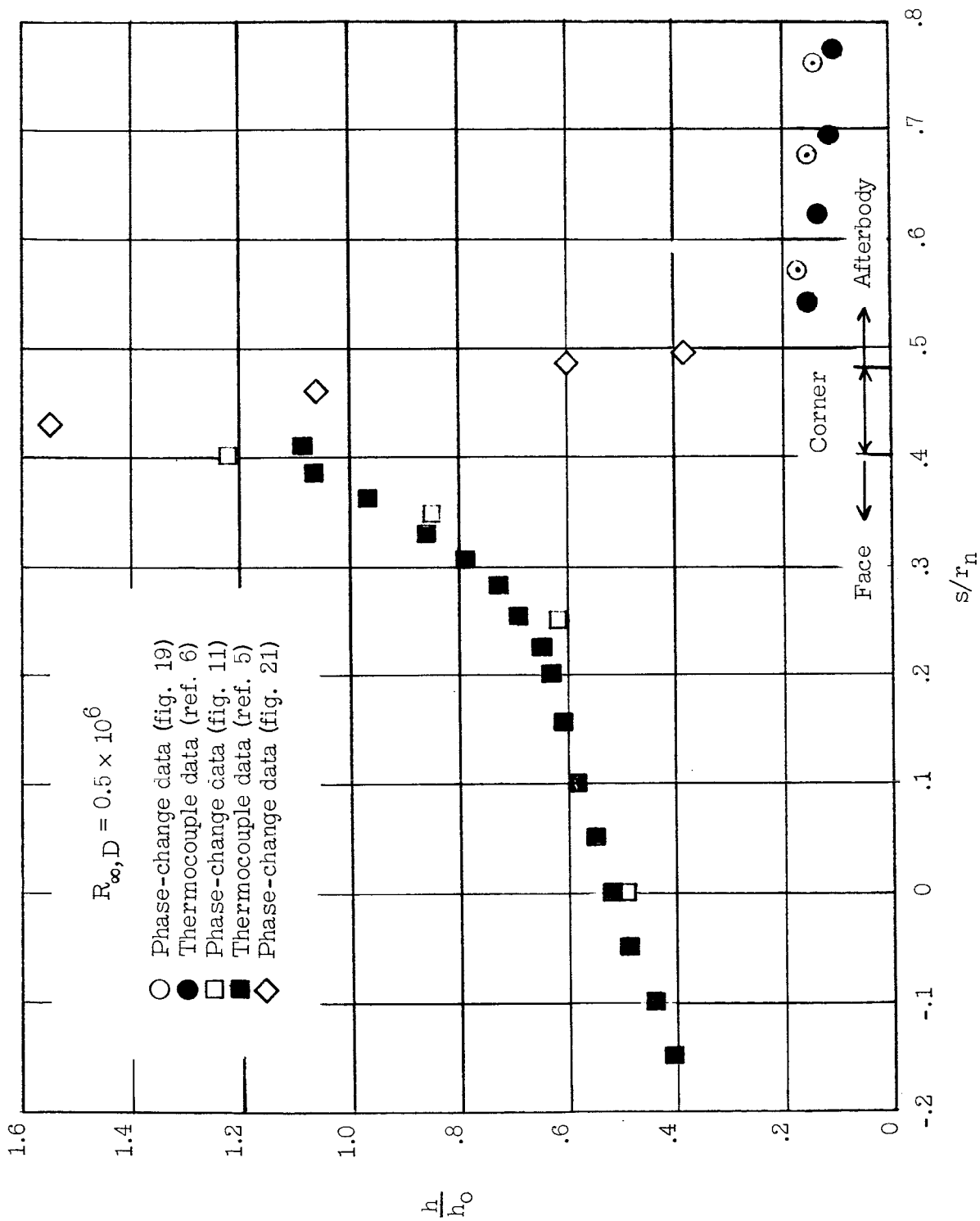
Figure 22.- Heat-transfer distribution for vertical plane of symmetry.
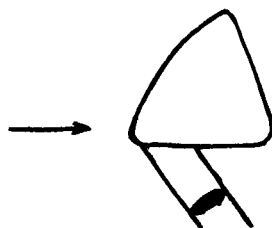
Thermocouple
configuration

Phase-change
configuration
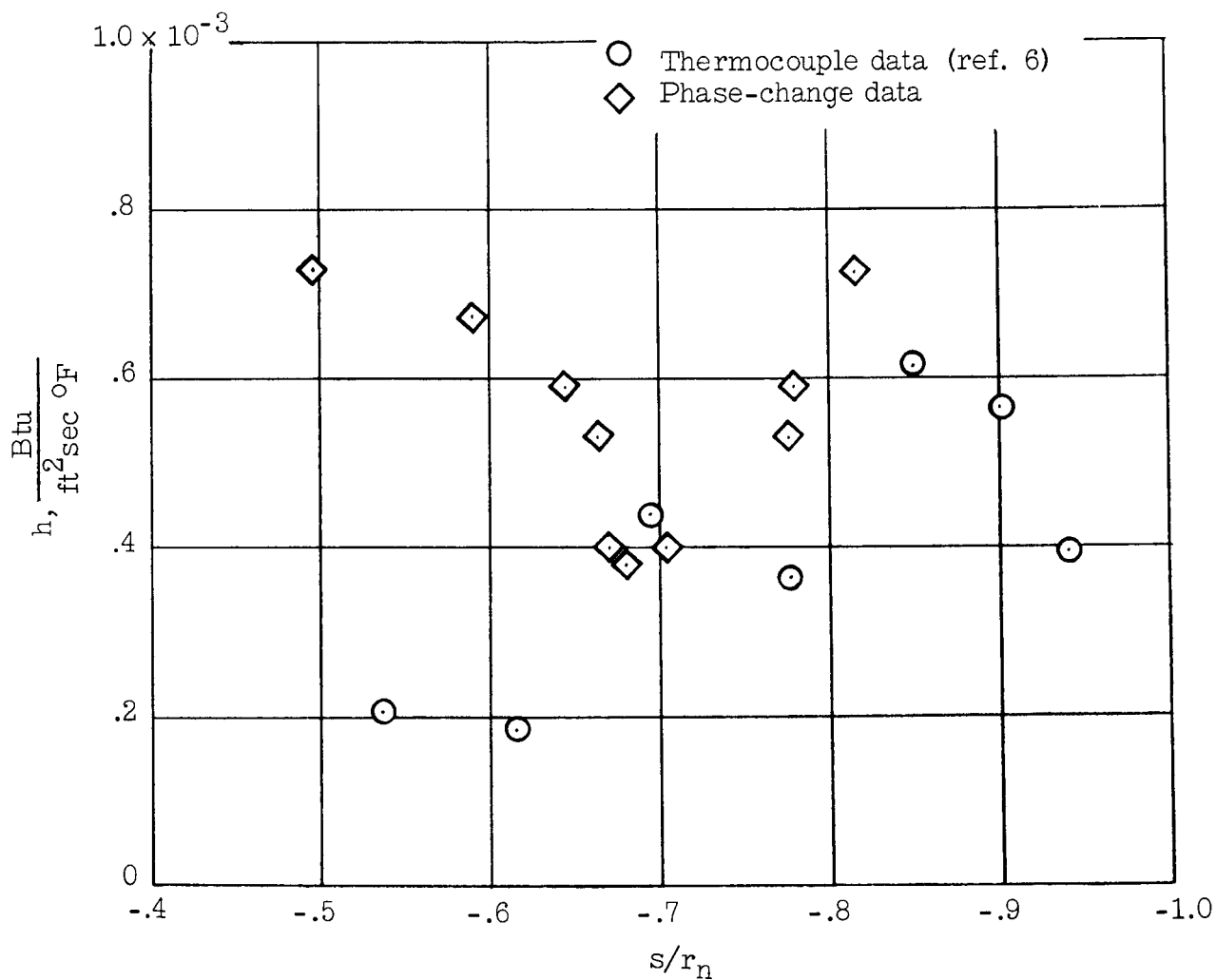
Figure 23.- Comparison of thermocouple-calorimeter and phase-change data for leeward
afterbody ray of smooth configuration. $R_{\infty,D} = 1.4 \times 10^6$.
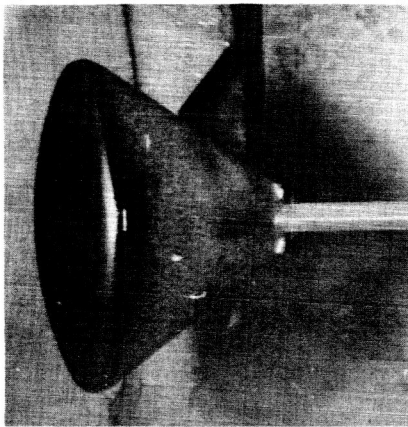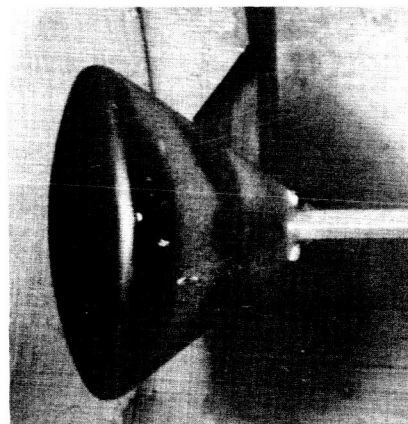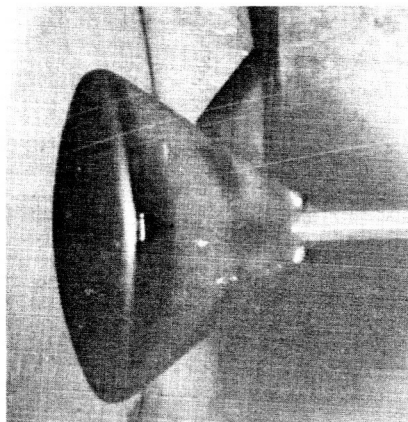
L-64-8373
Figure 24.- Photographs of heat-transfer patterns on smooth leeward afterbody. $R_{\infty,D} = 1.4 \times 10^6$.
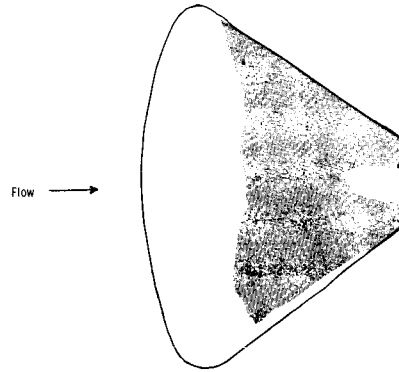
(a) $h = 7.25 \times 10^{-4}$; $\dfrac{h}{h_0} = 0.039$.
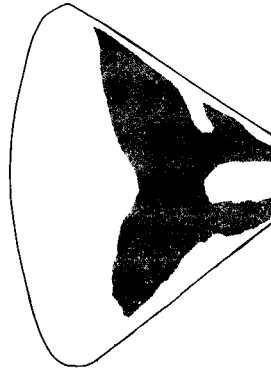
(b) $h = 6.71 \times 10^{-4}$; $\dfrac{h}{h_0} = 0.036$.
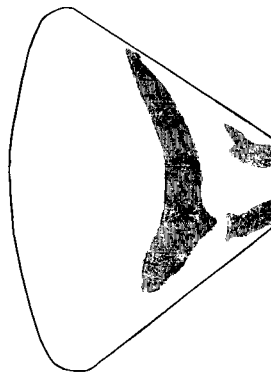
(c) $h = 5.35 \times 10^{-4}$; $\dfrac{h}{h_0} = 0.029$.

Figure 25.- Sketches of heat-transfer patterns on smooth leeward afterbody.

Flow →
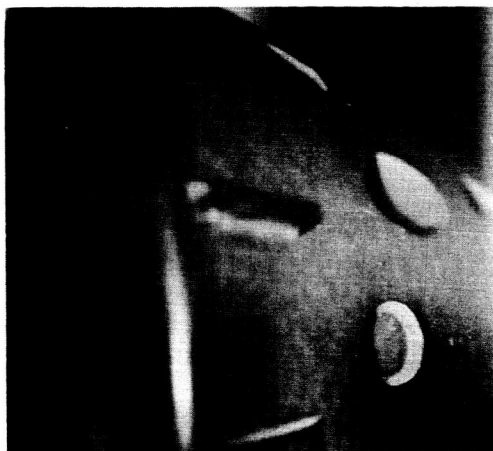
Increasing time
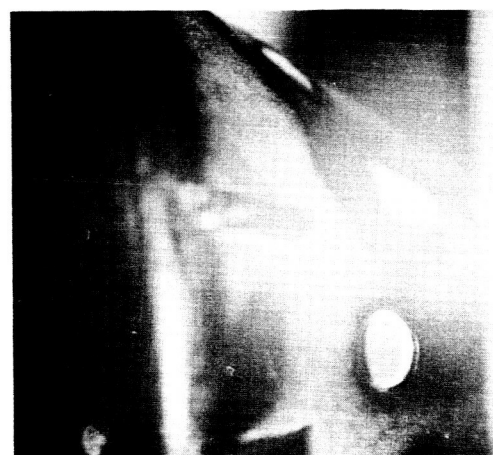
L-64-8374

Figure 26.- Photographs of patterns on leeward afterbody. Model 3; $R_{\infty, D} = 1.4 \times 10^6$.
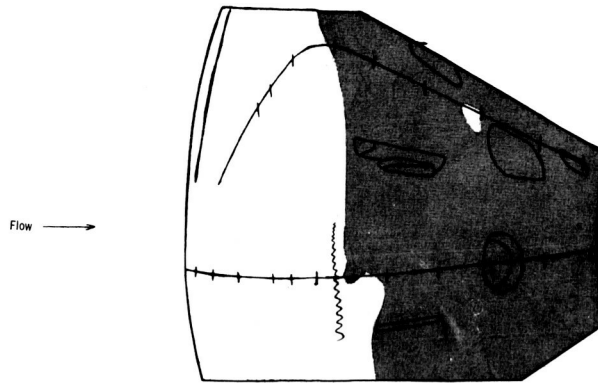
Flow ──→

(a) $h = 1.12 \times 10^{-3}$; $\dfrac{h}{h_0} = 0.060$.
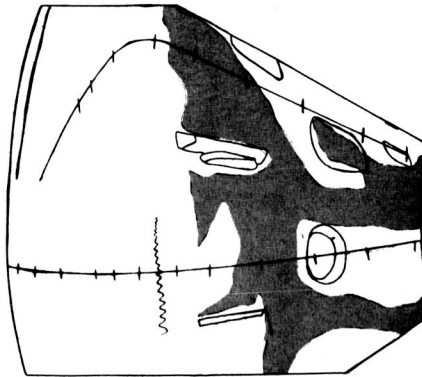
(b) $h = 6.44 \times 10^{-4}$; $\dfrac{h}{h_0} = 0.034$.
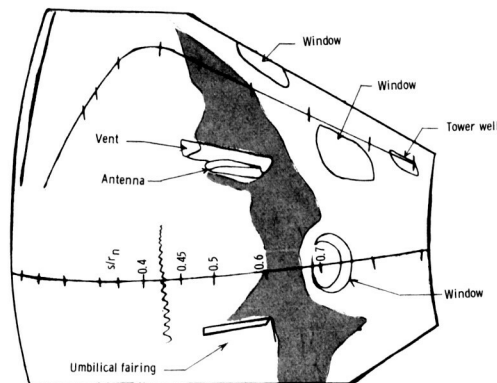
(c) $h = 5.45 \times 10^{-4}$; $\dfrac{h}{h_0} = 0.029$.

Figure 27.- Heat-transfer patterns on leeward afterbody. Model 3; $R_{\infty,D} = 1.4 \times 10^6$.
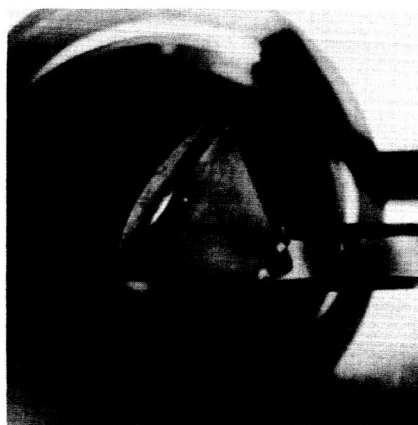
Flow ⟶

Increasing time

(a) Yaw jet.   L-64-8375

Figure 28.- Photographs of reaction-control patterns.

Flow

Increasing time

(b) Forward-firing roll jet.   L-64-8376

Figure 28.- Continued.
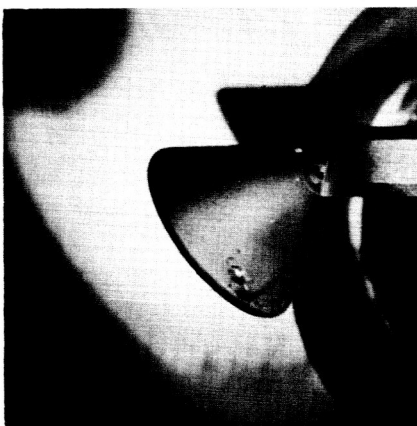
Flow ⟶

Increasing time

(c) Aft-firing roll jet.   L-64-8377

Figure 28.- Concluded.
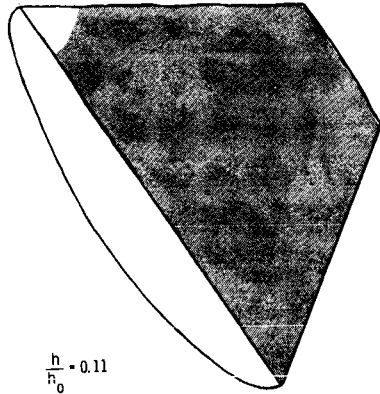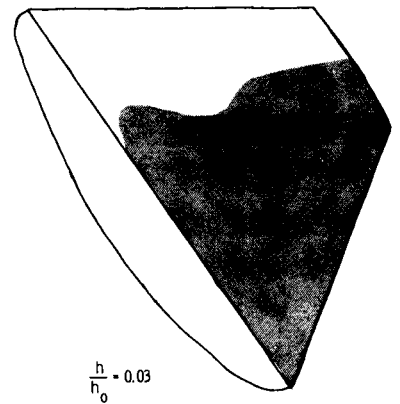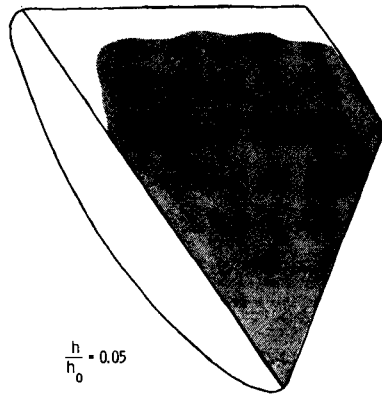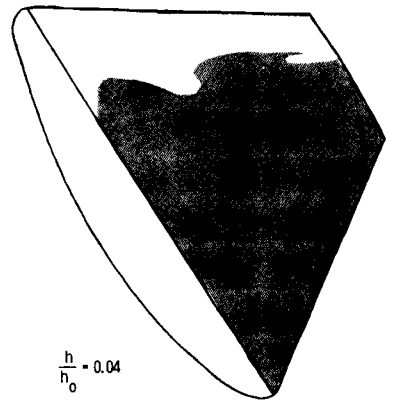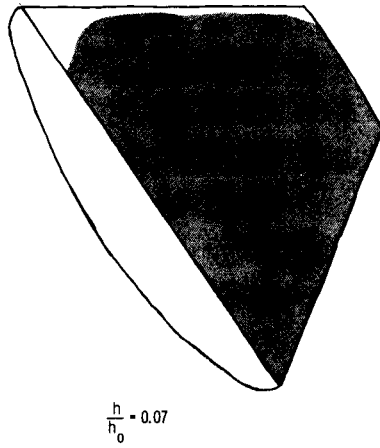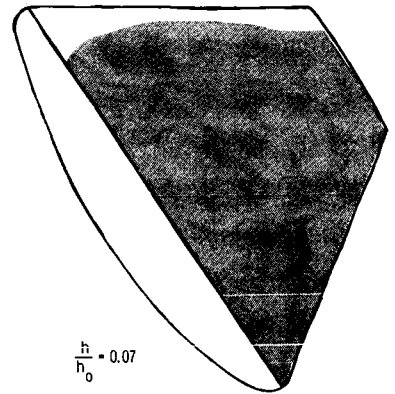
Figure 29.- Sketch of patterns on smooth afterbody. Side view.

$$\frac{h}{h_0} = 0.11 \qquad \frac{h}{h_0} = 0.07$$

$$\frac{h}{h_0} = 0.07 \qquad \frac{h}{h_0} = 0.04$$

$$\frac{h}{h_0} = 0.05 \qquad \frac{h}{h_0} = 0.03$$

(a) $R_{\infty,D} = 0.5 \times 10^6$.   (b) $R_{\infty,D} = 1.5 \times 10^6$.

Flow ⟶

(a) $\dfrac{h}{h_O} = 0.08$.


(b) $\dfrac{h}{h_O} = 0.06$.
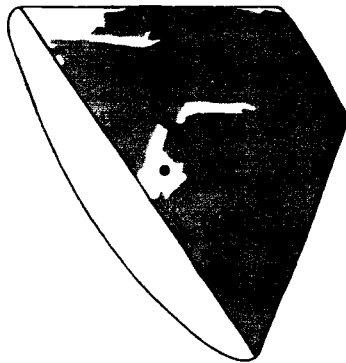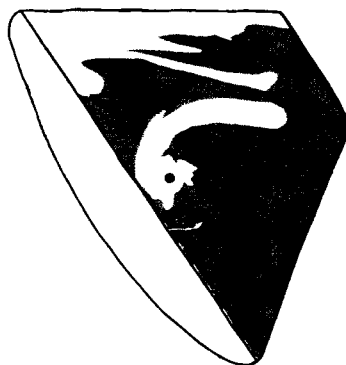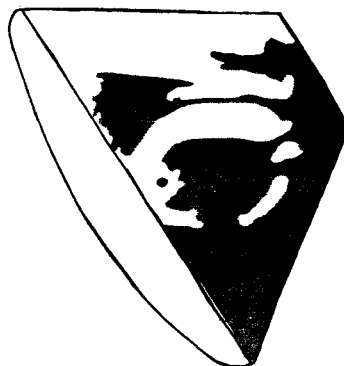
(c) $\dfrac{h}{h_O} = 0.04$.

Figure 30.- Sketch of patterns of yaw jet. $R_{\infty,D} = 1.5 \times 10^6$; throat = 0.08 inch.

Flow →

(a) $\dfrac{h}{h_o} = 0.07$.
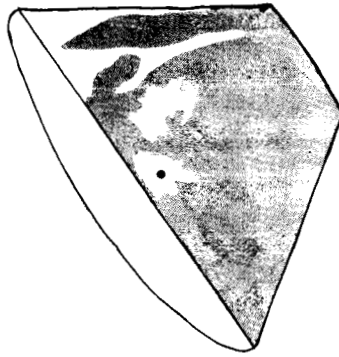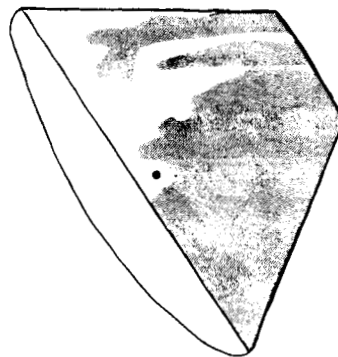
(b) $\dfrac{h}{h_o} = 0.06$.

Figure 31.- Sketch of patterns of yaw jet. $R_{\infty,D} = 0.13 \times 10^6$; throat = 0.08 inch.
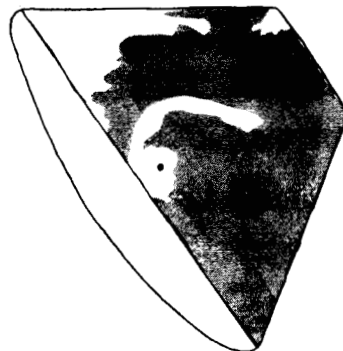
Flow →

Figure 32.- Sketch of patterns of yaw jet. $R_{\infty,D} = 0.13 \times 10^6$; throat = 0.02 inch; $\dfrac{h}{h_o} = 0.05$.

Flow →

(a) $\dfrac{h}{h_o}$ = 0.07.

(b) $\dfrac{h}{h_o}$ = 0.05.
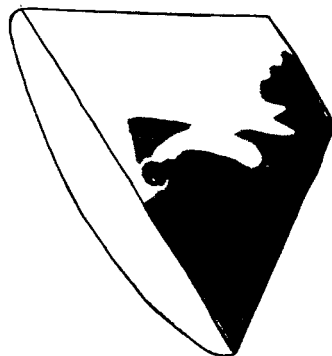
(c) $\dfrac{h}{h_o}$ = 0.03.

Figure 33.- Sketch of patterns of yaw jet. $R_{\infty,D}$ = 1.5 × 10^6; throat = 0.02 inch.
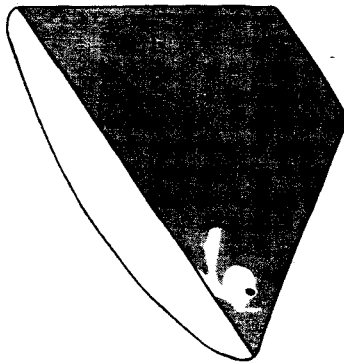
59
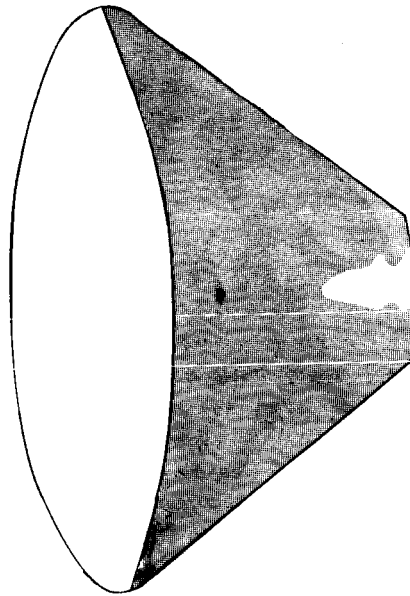
Flow $\longrightarrow$

(a) $\dfrac{h}{h_0} = 0.032$.

(b) $\dfrac{h}{h_0} = 0.026$.

Figure 34.- Sketch of patterns of pitch jet. $R_{\infty,D} = 1.5 \times 10^6$.

Flow →

(a) $\dfrac{h}{h_O} = 0.06$.

(b) $\dfrac{h}{h_O} = 0.05$.
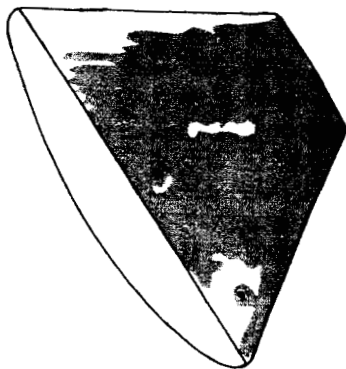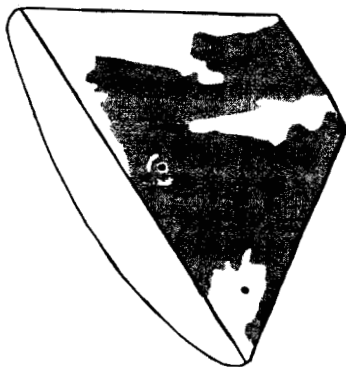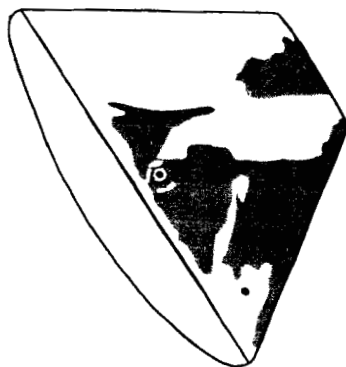
(c) $\dfrac{h}{h_O} = 0.035$.

Figure 35.- Sketch of patterns of yaw and forward-firing roll jet. $R_{\infty,D} = 1.5 \times 10^{-6}$.
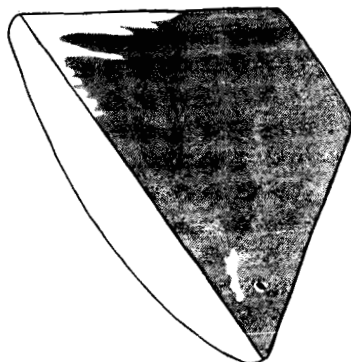
Flow ⟶
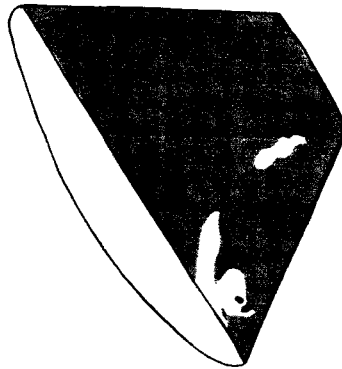
(a) $\dfrac{h}{h_0} = 0.07$.
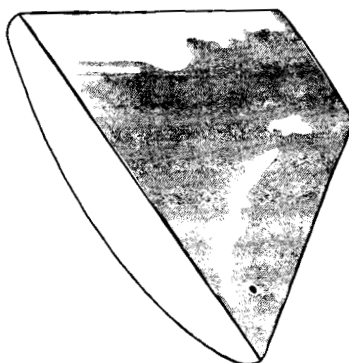
(b) $\dfrac{h}{h_0} = 0.05$.
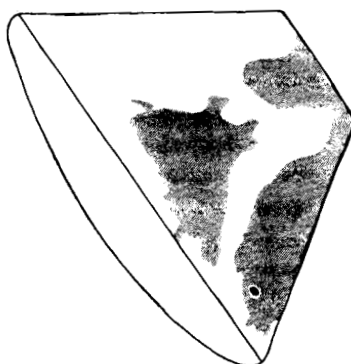
(c) $\dfrac{h}{h_0} = 0.03$.

Figure 36.- Sketch of patterns of forward-firing roll jet. $R_{\infty,D} = 1.5 \times 10^6$.
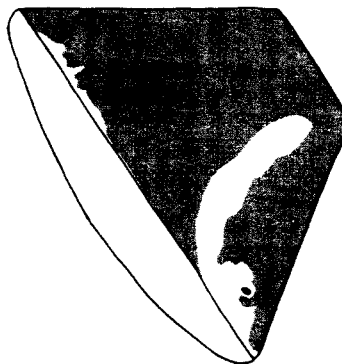
Flow ⟶

(a) $\dfrac{h}{h_0} = 0.15.$

(b) $\dfrac{h}{h_0} = 0.12.$

(c) $\dfrac{h}{h_0} = 0.08.$

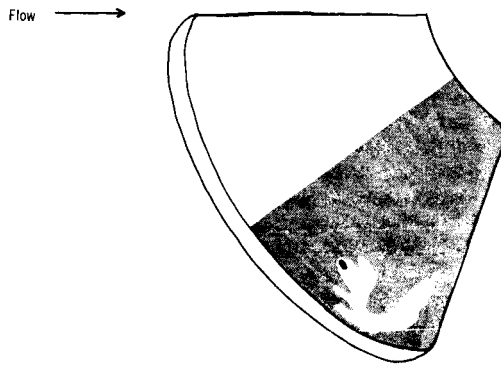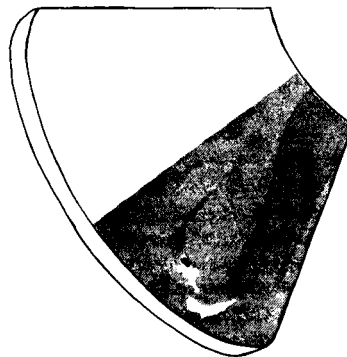Figure 37.- Sketch of patterns of forward-firing roll jet. $R_{\infty,D} = 0.13 \times 10^6.$
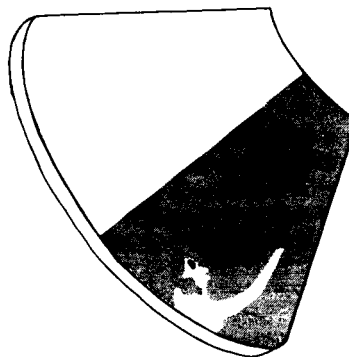
Figure 38.- Sketch of patterns of aft-firing roll jet. $R_{\infty,D} = 0.13 \times 10^6$; $\frac{h}{h_0} = 0.05$.

(a) $\frac{h}{h_0} = 0.05$.

(b) $\frac{h}{h_0} = 0.04$.

Figure 39.- Sketch of patterns of aft-firing roll jet. $R_{\infty,D} = 1.5 \times 10^6$.